Hierarchically-driven Approach for Quantifying Materials Uncertainty in Creep Deformation and Failure of Aerospace Materials

Andrew Oppedal
MISSISSIPPI STATE UNIVERSITY

07/01/2016
Final Report

REPORT DOCUMENTATION PAGE

1. REPORT DATE *(DD-MM-YYYY)*	2. REPORT TYPE	3. DATES COVERED *(From - To)*
30-06-2016	Final Report	1 April 2012 - 31 March 2016

4. TITLE AND SUBTITLE

Hierarchically-driven Approach for Quantifying Materials Uncertainty in Creep Deformation and Failure of Aerospace Materials

5a. CONTRACT NUMBER

FA9550-12-1-0135

5b. GRANT NUMBER

5c. PROGRAM ELEMENT NUMBER

6. AUTHOR(S)

Oppedal, Andrew L.

5d. PROJECT NUMBER

5e. TASK NUMBER

5f. WORK UNIT NUMBER

7. PERFORMING ORGANIZATION NAME(S) AND ADDRESS(ES)

Mississippi State University
Center for Advanced Vehicular Systems
Box 5405
Mississippi State, MS 39759

8. PERFORMING ORGANIZATION REPORT NUMBER

9. SPONSORING/MONITORING AGENCY NAME(S) AND ADDRESS(ES)

Multi-scale Structural Mechanics and Prognosis
Air Force Office of Scientific Research
875 North Randolph Street
Arlington, VA 22203-1768

10. SPONSOR/MONITOR'S ACRONYM(S)

11. SPONSOR/MONITOR'S REPORT NUMBER(S)

12. DISTRIBUTION/AVAILABILITY STATEMENT

Approved for Public Release; Distribution Unlimited

13. SUPPLEMENTARY NOTES

14. ABSTRACT

In collaboration with AFRL colleagues we have developed a methodology for measuring localized microstructure metrics in dendritic microstructures such as single crystal nickel-based superalloys, with potential application to a wide range of material systems. The primary dendrite arm spacing is correlated to processing (solidification rate), the microstructure of the material (interdentritic eutectic particles and voids), and properties (fatigue behavior and creep strength). In this project a Voronoi-based approach for spatial point pattern analysis has been applied to experimental and synthetic dendritic microstructures. This technique was used to quantify the distribution of local primary dendrite arm spacings, their spatial distribution, and their correlation with interdentritic eutectic particles. Several peer-reviewed journal articles, including an Editor's Choice article published in Metallurgical and Materials Transactions, and conference presentations describe this in more detail. Furthermore, to transfer this technology, a GUI based computational too has been developed to facilitate the use of these metrics in synthetic and experimental microstructures, with eventual application to link processing with structural properties based on the complex turbine blade microstructure.

15. SUBJECT TERMS

Primary dendrite arm spacing (PDAS), directionally solidified, microstructure, process-structure-property relationship, nickel-based superalloy

16. SECURITY CLASSIFICATION OF:			17. LIMITATION OF ABSTRACT	18. NUMBER OF PAGES	19a. NAME OF RESPONSIBLE PERSON
a. REPORT	b. ABSTRACT	c. THIS PAGE			
U	U	U	UU		19b. TELEPHONE NUMBER *(Include area code)*

INSTRUCTIONS FOR COMPLETING SF 298

1. REPORT DATE. Full publication date, including day, month, if available. Must cite at least the year and be Year 2000 compliant, e.g. 30-06-1998; xx-06-1998; xx-xx-1998.

2. REPORT TYPE. State the type of report, such as final, technical, interim, memorandum, master's thesis, progress, quarterly, research, special, group study, etc.

3. DATES COVERED. Indicate the time during which the work was performed and the report was written, e.g., Jun 1997 - Jun 1998; 1-10 Jun 1996; May - Nov 1998; Nov 1998.

4. TITLE. Enter title and subtitle with volume number and part number, if applicable. On classified documents, enter the title classification in parentheses.

5a. CONTRACT NUMBER. Enter all contract numbers as they appear in the report, e.g. F33615-86-C-5169.

5b. GRANT NUMBER. Enter all grant numbers as they appear in the report, e.g. AFOSR-82-1234.

5c. PROGRAM ELEMENT NUMBER. Enter all program element numbers as they appear in the report, e.g. 61101A.

5d. PROJECT NUMBER. Enter all project numbers as they appear in the report, e.g. 1F665702D1257; ILIR.

5e. TASK NUMBER. Enter all task numbers as they appear in the report, e.g. 05; RF0330201; T4112.

5f. WORK UNIT NUMBER. Enter all work unit numbers as they appear in the report, e.g. 001; AFAPL30480105.

6. AUTHOR(S). Enter name(s) of person(s) responsible for writing the report, performing the research, or credited with the content of the report. The form of entry is the last name, first name, middle initial, and additional qualifiers separated by commas, e.g. Smith, Richard, J, Jr.

7. PERFORMING ORGANIZATION NAME(S) AND ADDRESS(ES). Self-explanatory.

8. PERFORMING ORGANIZATION REPORT NUMBER. Enter all unique alphanumeric report numbers assigned by the performing organization, e.g. BRL-1234; AFWL-TR-85-4017-Vol-21-PT-2.

9. SPONSORING/MONITORING AGENCY NAME(S) AND ADDRESS(ES). Enter the name and address of the organization(s) financially responsible for and monitoring the work.

10. SPONSOR/MONITOR'S ACRONYM(S). Enter, if available, e.g. BRL, ARDEC, NADC.

11. SPONSOR/MONITOR'S REPORT NUMBER(S). Enter report number as assigned by the sponsoring/ monitoring agency, if available, e.g. BRL-TR-829; -215.

12. DISTRIBUTION/AVAILABILITY STATEMENT. Use agency-mandated availability statements to indicate the public availability or distribution limitations of the report. If additional limitations/ restrictions or special markings are indicated, follow agency authorization procedures, e.g. RD/FRD, PROPIN, ITAR, etc. Include copyright information.

13. SUPPLEMENTARY NOTES. Enter information not included elsewhere such as: prepared in cooperation with; translation of; report supersedes; old edition number, etc.

14. ABSTRACT. A brief (approximately 200 words) factual summary of the most significant information.

15. SUBJECT TERMS. Key words or phrases identifying major concepts in the report.

16. SECURITY CLASSIFICATION. Enter security classification in accordance with security classification regulations, e.g. U, C, S, etc. If this form contains classified information, stamp classification level on the top and bottom of this page.

17. LIMITATION OF ABSTRACT. This block must be completed to assign a distribution limitation to the abstract. Enter UU (Unclassified Unlimited) or SAR (Same as Report). An entry in this block is necessary if the abstract is to be limited.

Hierarchically-driven Approach for Quantifying Materials Uncertainty in Creep Deformation and Failure of Aerospace Materials

Andrew L. Oppedal

Mississippi State University

June 30, 2016

Abstract

In collaboration with AFRL colleagues we have developed a methodology for measuring localized microstructure metrics in dendritic microstructures such as single crystal nickel-based superalloys, with potential application to a wide range of material systems. The primary dendrite arm spacing is correlated to processing (solidification rate), the microstructure of the material (interdentritic eutectic particles and voids), and properties (fatigue behavior and creep strength). In this project a Voronoi-based approach for spatial point pattern analysis has been applied to experimental and synthetic dendritic microstructures. This technique was used to quantify the distribution of local primary dendrite arm spacings, their spatial distribution, and their correlation with interdentritic eutectic particles. Several peer-reviewed journal articles, including an Editor's Choice article published in Metallurgical and Materials Transactions, and conference presentations describe this in more detail. Furthermore, to transfer this technology, a GUI based computational too has been developed to facilitate the use of these metrics in synthetic and experimental microstructures, with eventual application to link processing with structural properties based on the complex turbine blade microstructure.

Contents

List of Figures

Acknowledgments

1 Final Project Summary

The following section includes details of the proposal and program plans for the AFOSR project.

1.1 Research Effort

This 3-year research project qualitatively and quantitatively mapped the relationship between the hierarchical microstructure and the elevated temperature creep deformation and failure behavior of single crystal nickel-based superalloys. This research established a methodology for incorporating microstructure-based structure-property relationships into mechanics-based material models and answering questions related to "how microstructural features alter localized deformation at elevated temperatures" and "what is the materials uncertainty associated with elevated temperature creep deformation" for developing the next generation of elevated temperature structural materials for propulsion systems applications through materials-based design approaches.

On a large scale, a problem central to designing the next generation propulsion systems for the USAF is that the present length of time required for new material design is much larger than the timelines required for development of commercial engines and engine components. At the Superalloys 2008 conference, the keynote address postulated that the grand challenge for materials development is to drastically reduce this development time for new materials and processes without adding development risk. Indeed, accelerating the pace of discovery, development, manufacturing, and deployment of advanced materials systems has been described as crucial to achieving global competitiveness in the 21st century in a "Materials Genome Initiative" white paper recently released by the White House's National Science and Technology Council. Moreover, recent discussions and reports on integrated computational materials engineering (ICME) provide a conceptual roadmap for how to design materials, but the community also agrees that there are still a number of challenges that must be addressed before ICME reaches its full potential. Nevertheless, success stories in the automotive and aerospace sectors show that the aforementioned grand challenge is solvable.

Accelerating the pace of discovery requires physically-based models that describe the "processing-structure-property-performance" relationships. As Figure 1 shows, these models require information about how material processing/chemistry relates to structure, how structure relates to properties, and how properties ultimately relate to the performance of a specific component for a particular application. As an example, the γ' precipitate microstructure (structure, left) is shown in Figure 1 with results from elevated temperature creep testing (property, right). The structure-property relationship (middle) captures the link between the volume fraction of γ' precipitates and creep

1

rupture life. Quantifying these relationships is invaluable both for designing new materials and for optimizing the properties/performance of existing materials. Developing the models, databases, and tools for developing these relationships will help establish the infrastructure required to solve this complex engineering problem.

On a smaller scale, a relevant problem for the USAF is that increasingly higher temperatures and pressures in the high pressure turbine section of the modern turbine engine leads to a steep decrease in properties at temperatures above 850 °C for single crystal nickel-based superalloys. However, to solve this specific problem requires developing mechanics-based material models with uncertainty that can capture the appropriate structure-property relationships by: (1) measuring details of the hierarchical microstructure and its evolution and (2) relating this to properties at elevated temperatures under extreme conditions (i.e., creep, low- and high-cycle fatigue, fretting, embrittlement, and environment effects). In this sense, these models will relate the initial material
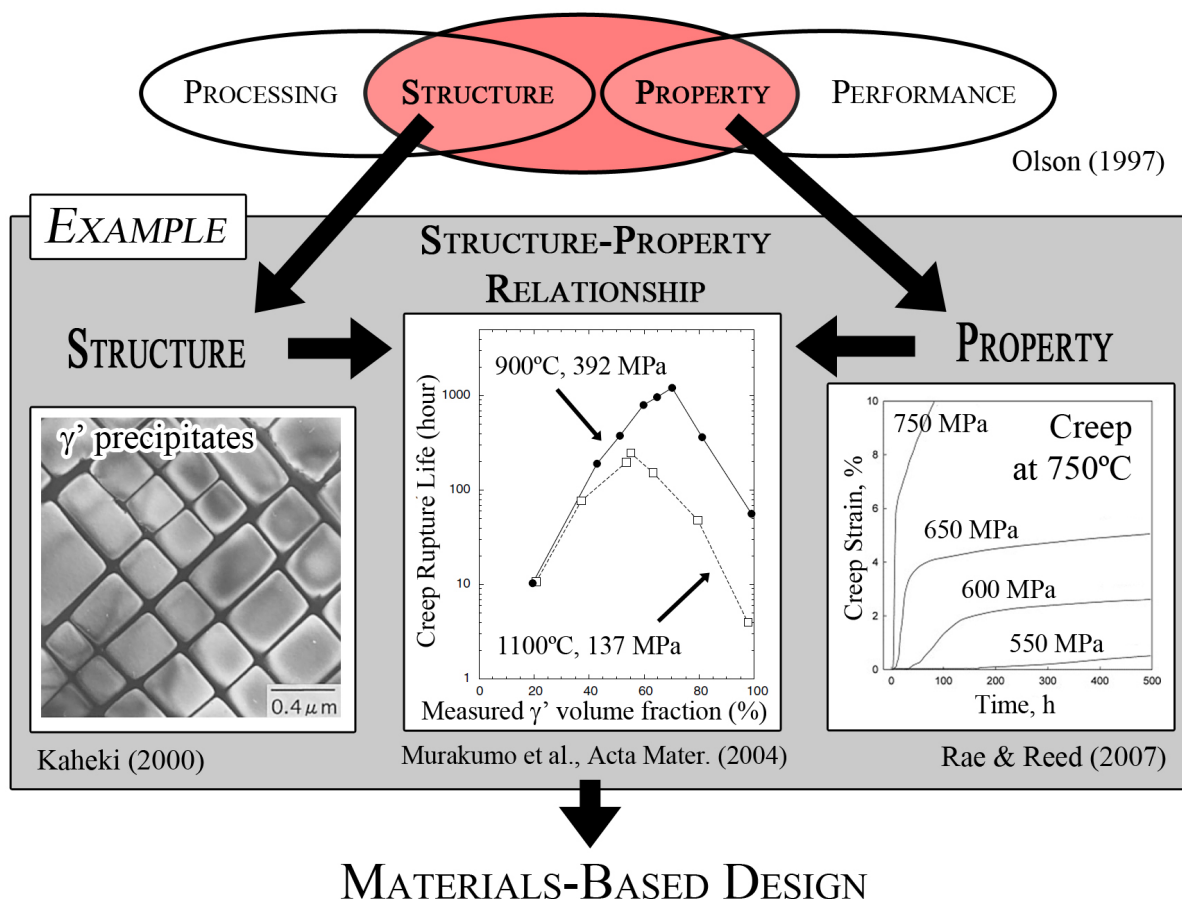

Figure 1. Schematic of the "processing-structure-property-performance" materials design concept. The proposed research will focus on structure-property relationships in single crystal Ni-based superalloys for materials-based design. The example shows how precipitate volume fraction affects creep rupture life.

microstructure to the properties that ultimately influence performance of components and systems. To do so requires that the relevant features and their variability are captured via statistical descriptors. Moreover, the relationship between structure and properties must be firmly established and carefully validated with experiments in order to not increase development risk. There are multiple challenges to developing microstructure-based predictive models and intrinsically coupling with variability associated with microstructure heterogeneities:

1. What metrics should be used to describe a digital representation of material microstructure? How does airfoil geometry (processing) affect microstructure? What is the uncertainty associated with microstructure statistics (i.e., representative volume size)? How does material microstructure evolve during service?

2. How does microstructure feature heterogeneity relate to local deformation character? Can in-situ experiments be used to provide local structure-property relationships? How does the microstructure affect cumulative damage during elevated temperature deformation?

3. What is the link between extreme values of creep rupture life and microstructure? What is the materials uncertainty associated with creep properties? Can this be related to the local microstructure?

To address these challenges, this research uses a combination of microscopy and elevated temperature mechanical testing, combined with computational approaches. Here, a unique, multipronged approach is pursued to understand the role of material microstructure and their associated uncertainties on the deformation behavior of aerospace materials at a number of length scales that span from the macroscale (homogeneous microstructure and properties) to the microscale (containing resolution of individual microstructure features). In particular, this research uses Air Force-relevant single crystal nickel-based superalloys to explore the influence of microstructure on creep deformation.

1.2 Significance and Relevance to USAF

Single crystal nickel turbine blades are being utilized in turbine jet engines throughout industry because of their superior creep, stress rupture, melt resistance, and thermomechanical fatigue capabilities over polycrystalline alloys. With respect to its significance to the USAF, single crystal alloys are used for turbine blades within the high pressure turbine (HPT) section of turbine engines, e.g., in the GE F110 engine. The F110 turbine engine has been the engine of choice for the F-16 since there was an engine choice for that aircraft; fully 86% of the USAF F-16C/Ds and 75% of all front line, combat-coded F-16s are powered by the GE F110. Part of the motivation for choosing

this particular alloy class is that the limiting factor for specific thrust within the turbine engine is the temperature of the turbine section (where the single crystal turbine blades reside). Thus, a fundamental understanding of the hierarchical microstructure influences that contribute to failure can contribute to both an improvement in the ability to predict life in these systems as well as the potential to re-engineer these alloys or redesign the components for improved elevated temperature properties and propulsion system efficiency.

As the operating temperatures in the hot section of the turbine engine continue to increase, the airfoil design and geometry is becoming increasingly complex - wall thicknesses are decreasing and cooling passages are more intricate to keep the turbine blade cool. Therefore, it has become even more vital to understand how microstructure affects high temperature properties as wall thicknesses and geometry within the airfoil approach the length scales of some of the microstructure features themselves. This proposal will utilize experiments for testing specimens that are on the order of the wall thickness of turbine blades, as it has previously been found that specimen thickness plays a commanding role in elevated temperature creep properties. Creep deformation testing is especially relevant because the severe loads experienced in long cruise missions have a large fraction of hot dwell time. Again, this testing is motivated by mission conditions experienced by thin sections within HPT blades.

1.3   Final Report Summary of Accomplishments

The summary and accomplishments of the current AFOSR project is as follows:

1. In collaboration with AFRL colleagues, we have developed a methodology for measuring localized microstructure metrics in dendritic microstructures (e.g., single crystal nickel-based superalloys), with potential application to order/disorder in a wide range of material systems. Characterizing the primary dendrite arm spacing in directionally-solidified microstructures is an important step for developing process-structure-property relationships by enabling the quantification of (i) the influence of processing on microstructure and (ii) the influence of microstructure on properties. Thin-walled directionally-solidified structures (e.g., a turbine blade) require new approaches for characterizing the dendrite arm spacing and the microstructure. In this work, we utilized a new Voronoi-based approach for spatial point pattern analysis that was applied to an experimental dendritic microstructure. This technique utilizes a Voronoi tessellation of space surrounding the dendrite cores to determine nearest neighbors and the local primary dendrite arm spacing. In addition, we compared this technique to a recent distance-based technique, the Warnken–Reed method, and a modification to this using Voronoi tessellations, along with the minimal spanning tree method. Moreover, a convex hull-based technique was used to include edge effects for such techniques, which can be important for

4

thin specimens. These methods were used to quantify the distribution of local primary dendrite arm spacings as well as their spatial distribution for an experimental directionally-solidified superalloy micrograph. Last, eutectic particles were segmented to correlate distances from dendrite cores and Voronoi vertices to the occurrence and size of these interdendritic features. Interestingly, with respect to the distance from the dendrite core, it was found that there is a greater probability of occurrence of large eutectic particles ($> 410 \, \mu$m) over small particles at distances greater than approximately $1/3$ of the bulk-measured primary dendrite arm spacing. This systematic study of the different techniques for quantifying local primary dendrite arm spacings, and their effect on microstructure, can be an important step for correlating with both processing and properties in single crystal nickel-based superalloys.

2. Furthermore, to transfer this technology, a GUI-based computational tool has been developed to facilitate the use of these metrics in synthetic and experimental microstructures, with eventual application to link processing with structural properties based on the complex turbine blade microstructure. This tool is being used to examine the uncertainty with various methods for measuring local microstructure characteristics and to examine the sensitivity of using such techniques for evaluating microstructure. In addition to the GUI tool, a manual describing its use has been produced and will be released along with the tool after publication of the first combined study with synthetic and experimental microstructures (anticipated Fall 2014). Additionally, further techniques for characterizing microstructure, such as the minimal spanning tree methodology, were explored in collaboration with Kiran Solanki at Arizona State University.

3. At the Army Research Laboratory (ARL) where the original PI for this project, Mark A. Tschopp, is a researcher now, a small scale (down to 150-μm diameter) high temperature (<1200 °C) shear punch tester was built to examine the utility of rapid, small-volume, high temperature creep uncertainty studies on aerospace alloys. As most creep tests can take several days on bulk specimens, this may allow for more rapid capability for assessing Larson–Miller plots as well as providing the potential capability to examine the creep response in very thin sections such as in the actual turbine blade.

4. Mark A. Tschopp was the lead organizer for a symposium on "Multi-scale Microstructure, Mechanics & Prognosis of High Temperature Alloys" for TMS 2015 (March 15–19, 2015 in Orlando, Florida) with co-organizers Jeffrey Evans, Jonathan Cormiér, and Qiang (Charles) Feng. This symposium was sponsored by the High Temperature Alloys Committee and was co-sponsored by the Computational Materials Science committee and the Mechanical Behavior of Materials committee. There were 62 presentations in this symposium, including one from authors on this project.

5. Some of the results of this work have been featured in an Editor's Choice article published in Metallurgical and Materials Transactions as well as multiple talks, most notably invited talks at the annual TMS 2013 and ASME IMECE 2013 conferences.

6. Additionally, recent discussions with the Propulsion branch at the Army Research Laboratory may help in establishing future opportunities for collaboration between the Army and the Air Force in the area of high temperature aerospace materials research.

1.4 Papers and Presentations delivered

Peer Reviewed, Archived Journal Articles

1. M.A. Tschopp, A.L. Oppedal, J.D. Miller, M.A. Groeber, A.H. Rosenberger, K.N. Solanki, Characterizing primary dendritic microstructures to quantify the processing-structure-property relationship in single crystal nickel-based superalloys, ed. J. Y. Hwang, C. Bai, J. Carpenter, S. Ikhmayies, B. Li, N. Monteiro, Z. Peng, M. Zhang, Characterization of Minerals, Metals, and Materials 2013, TMS (The Minerals, Metals, & Materials Society), 2013: pp. 301–310.

2. This paper was selected as an Editor's Choice as having special significance.

   M.A. Tschopp, J.D. Miller, A.L. Oppedal, K.N. Solanki, Characterizing the Local Primary Dendrite Arm Spacing in Directionally Solidified Dendritic Microstructures, Metallurgical and Materials Transactions A. 45 (2014) 426–437.

3. M.A. Tschopp, J.D. Miller, A.L. Oppedal, K.N. Solanki, Evaluating Local Primary Dendrite Arm Spacing Characterization Techniques Using Synthetic Directionally Solidified Dendritic Microstructures, Metallurgical and Materials Transactions A. 46 (2015) 4610–4628.

 Peer Reviewed Abstract, Invited Presentation

1. M.A. Tschopp, A.L. Oppedal, J.D. Miller, M.A. Groeber, A.H. Rosenberger, K.N. Solanki, Characterizing primary dendritic microstructures to quantify the processing-structure-property relationship in single crystal nickel-based superalloys, in: TMS 2013 Annual Meeting, March 3–7, 2013, San Antonio, TX

2. M.A. Tschopp, A.L. Oppedal, J.D. Miller, M.A. Groeber, A.H. Rosenberger, K.N. Solanki, Understanding the Processing-Structure-Property Relationships in Single Crystal Nickel-Based Superalloys, in ASME 2013 International Mechanical Engineering Congress, November 15–21, 2013, San Diego, CA

3. M.A. Tschopp, A.L. Oppedal, K.N. Solanki, Local/Global Measurement of Primary Dendrite Arm Spacing in Single Crystal Nickel-Based Superalloys,in: TMS 2015 Annual Meeting, March 15–19, 2013, Orlando, FL

 Program Review Meetings

1. M.A. Tschopp, A.L. Oppedal, S. Turnage, (Poster) Hierarchically-driven approach for quantifying materials uncertainty in creep deformation and failure of aerspace materials, Multi-scale Structural Mechanics and Prognosis Awardee Review Meeting, July 25, 2012, Washington, DC

2. M.A. Tschopp, A.L. Oppedal, R. Carino, S. Turnage, K. N. Solanki, (Presentation) Hierarchically-driven approach for quantifying materials uncertainty in creep deformation and failure of aerspace materials, Multi-scale Structural Mechanics and Prognosis Awardee Review Meeting, July 24, 2013, Washington, DC

3. M.A. Tschopp, A.L. Oppedal, R. Carino, S. Turnage, K. N. Solanki, (Presentation) Hierarchically-driven approach for quantifying materials uncertainty in creep deformation and failure of aerspace materials, Multi-scale Structural Mechanics and Prognosis Awardee Review Meeting, September 5, 2014, Albuquerque, NM

Characterizing the Local Primary Dendrite Arm Spacing in Directionally Solidified Dendritic Microstructures

MARK A. TSCHOPP, JON D. MILLER, ANDREW L. OPPEDAL, and KIRAN N. SOLANKI

Characterizing the spacing of primary dendrite arms in directionally solidified microstructures is an important step for developing process–structure–property relationships by enabling the quantification of (i) the influence of processing on microstructure and (ii) the influence of microstructure on properties. In this work, we utilized a new Voronoi-based approach for spatial point pattern analysis that was applied to an experimental dendritic microstructure. This technique utilizes a Voronoi tessellation of space surrounding the dendrite cores to determine nearest neighbors and the local primary dendrite arm spacing. In addition, we compared this technique to a recent distance-based technique and a modification to this using Voronoi tessellations. Moreover, a convex hull-based technique was used to include edge effects for such techniques, which can be important for thin specimens. These methods were used to quantify the distribution of local primary dendrite arm spacings, their spatial distribution, and their correlation with interdendritic eutectic particles for an experimental directionally solidified Ni-based superalloy micrograph. This can be an important step for correlating processing and properties in directionally solidified dendritic microstructures.

I. INTRODUCTION

DEVELOPING an enhanced understanding of mechanical behavior in materials relies upon sufficiently characterizing microstructure details at the relevant length scales that contribute to this behavior. Moreover, to truly enhance the predictive capability of processing–structure–property models that aim to improve material performance requires a quantitative stereological description of the relevant microstructure features and, thereby, the material itself. Predictive models that effectively capture the linkage between processing and properties (through microstructure) can be utilized within an integrated computational materials engineering (ICME) approach to design materials and accelerate their insertion into application.

The focus of the present work is on single-crystal nickel-based superalloys, which are used in turbine blades within the high temperature section of the modern turbine engine.[1,2] In single-crystal nickel-based superalloys, there are a number of length scales of microstructure that contribute to mechanical behavior, ranging from the γ' precipitates to pores and eutectic particles to the dendrites themselves. At the largest microstructure length scale in directionally solidified single-crystal microstructures, the features of interest are the dendrites; many features at lower length scales (e.g., eutectic particles, precipitates, etc.) or at similar scales (e.g., porosity, freckle defects, etc.) are strongly associated with the dendrite arm spacing and morphology.[3–7] The solidification morphology associated with dendrite arm spacing has been described in the literature.[8,9] Historically, the primary dendrite arm spacing (PDAS) has been found to correlate with processing (e.g., solidification rate)[7,10–14] as well as with properties (e.g., creep strength, fatigue properties).[15,6] For instance, Lamm and Singer[6] produced single-crystal nickel-based microstructures (PWA 1483) with a varied range of different dendrite arm spacings (250 to 600 μm) and found that decreasing the mean dendrite arm spacing was associated with an increased high-cycle fatigue life. The fatigue cracks were found to originate at shrinkage porosity and the largest pores correlated with a large PDAS.

The traditional approach for measuring PDAS in single-crystal metals, whereby the number of dendrite cores in a specified area is related to the dendrite arm spacing[10,16,17] is given by:

$$\lambda = c\sqrt{\frac{A}{n}}, \qquad [1]$$

where λ is PDAS, A is the area analyzed, n is the number of dendrites, and c is a coefficient that depends on the microstructure. McCartney and Hunt[10] showed that $c = 0.5$ for a random array of points, $c = 1$ for a

MARK A. TSCHOPP, Senior Research Scientist, is with the Lightweight and Specialty Metals Branch, Materials and Manufacturing Science Division, Army Research Laboratory, Aberdeen Proving Ground, MD 21005, and also with the Center for Advanced Vehicular Systems, Mississippi State University, Starkville, MS 39759. Contact e-mail: mark.a.tschopp.ctr@mail.mil JON D. MILLER, Senior Materials Research Engineer, is with the Air Force Research Laboratory, Wright-Patterson AFB, Dayton, OH 45433. ANDREW L. OPPEDAL, Postdoctoral Associate, is with the Center for Advanced Vehicular Systems, Mississippi State University. KIRAN N. SOLANKI, Assistant Professor, is with the School for Engineering of Matter, Transport, and Energy, Arizona State University, Tempe, AZ 85287.
Manuscript submitted June 14, 2013.
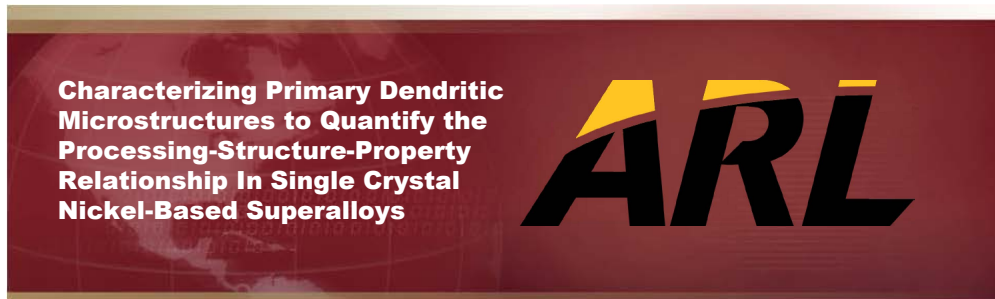Article published online September 17, 2013

Figure 2. Example peer-reviewed journal publication published in the current AFOSR project.

Figure 3. Example invited presentation on materials characterization for superalloys delivered at national and international professional society conferences.

Figure 4. Example Multi-scale Structural Mechanics and Prognosis Awardee Review presentation .

Meeting: 2015 TMS Annual Meeting & Exhibition

Symposium:
Multi-scale Microstructure, Mechanics & Prognosis of High Temperature Alloys

Sponsorship:
High Temperature Alloys Committee (Sponsor)
Mechanical Behavior (co-Sponsor), Computational Materials Science (co-Sponsor)

Organizers:
Mark A. Tschopp, U.S. Army Research Laboratory
Jeffrey L. Evans, University of Alabama in Huntsville
Jonathan Cormier, Ecole Nationale Supérieure de Mécanique et d'Aérotechnique (ENSMA), France
Qiang (Charles) Feng, University of Science and Technology Beijing (USTB), China

Scope:
A number of critical applications in industry demand the use of high temperature alloys that can withstand various extreme environments under elevated temperature conditions. Reliably predicting the life of these components, which may be subjected to damage associated with creep deformation, cyclic loading, environmental degradation, and combinations thereof, is a challenging endeavor. Under these conditions, the state of the microstructure after processing and its evolution during service lead to damage mechanisms that manifest over multiple length scales, ranging from quantum and atomistic scales to the mesoscale to the macroscale.

This symposium will provide a venue for presenting recent achievements in understanding the microstructure evolution and mechanical behavior in high temperature alloys over multiple scales in order to ultimately predict the prognosis and life of components. Advances in experimental and computational capability have greatly improved our ability to understand and quantify deformation mechanisms in high temperature alloys. In particular, a goal of this symposium is to accelerate the development and acceptance of new methodologies for improving prognosis through understanding the fundamental relationships between material microstructure and mechanical behavior in these alloys. It is expected that this symposium will include talks ranging from atomistic, discrete dislocation, and continuum mechanics approaches for various length scales as well as experimental mechanics results that elucidate the behavior of these alloys.

The subject areas of this symposium include, but are not limited to:
- Multi-scale modeling of high temperature deformation and damage
- Single crystal and polycrystal plasticity models
- Deformation and damage based life prediction techniques
- Modeling and experimental approaches to creep-fatigue-environment interactions
- Discrete dislocation dynamics and mesoscale (phase field) modeling of creep deformation
- Experimental methods for materials prognosis and structural health monitoring
- Understanding and quantifying microstructure-property relationships at high temperature
- Computational and experimental approaches for accelerated materials design of high temperature alloys
- Effect of chemistry and processing on high temperature structure and properties

Figure 5. Symposium on high temperature microstructure and mechanics of aerospace materials organized for TMS 2015.

2 TMS Conference Paper, March 2013

M.A. Tschopp, A.L. Oppedal, J.D. Miller, M.A. Groeber, A.H. Rosenberger, K.N. Solanki, Characterizing primary dendritic microstructures to quantify the processing-structure-property relationship in single crystal nickel-based superalloys, ed. J. Y. Hwang, C. Bai, J. Carpenter, S. Ikhmayies, B. Li, N. Monteiro, Z. Peng, M. Zhang, Characterization of Minerals, Metals, and Materials 2013, TMS (The Minerals, Metals, & Materials Society), 2013: pp. 301–310.

CHARACTERIZING PRIMARY DENDRITIC MICROSTRUCTURES TO QUANTIFY THE PROCESSING-STRUCTURE-PROPERTY RELATIONSHIP IN SINGLE CRYSTAL NICKEL-BASED SUPERALLOYS

M.A. Tschopp[1,2], A.L Oppedal[2], J.D. Miller[3], M.A. Groeber[3], A.H. Rosenberger[3], K.N. Solanki[4]

[1] Oak Ridge Institute for Science and Education; Army Research Laboratory, APG, MD, 21014

[2] Center for Advanced Vehicular Systems; Mississippi State University, Starkville, MS 39759

[3] Air Force Research Laboratory, WPAFB, OH 45433

[4] School for Engineering of Matter, Transport, and Energy, Arizona State University, Tempe, AZ 85287

Email address: mark.a.tschopp.ctr@mail.mil

Keywords: Dendrite Arm Spacing, Superalloy, Structure-Property Relationship

Abstract

Characterizing the spacing of primary dendrite arms in directionally-solidified microstructures is an important step for developing process-structure-property relationships by enabling the quantification of (i) the influence of processing on microstructure and (ii) the influence of microstructure on properties. The research objective herein is to evaluate the capability of various conventional approaches, as well as new or modified approaches, for spatial point pattern analysis with application to characterizing experimental dendritic microstructures. Both computer-generated and experimental dendritic microstructures are used for this analysis along with numerous techniques based on the nearest neighbor spacing, Voronoi tessellation, Delaunay triangulation, or graph theory. Comparison of new metrics with traditional primary dendrite arm spacing metrics will also be discussed for both local and global measures. The current methods investigated will supply information of local spacing and coordination number while addressing edge effects, parameter sensitivity, and correlation with interdendritic features, thus providing insight into how processing affects properties.

Introduction

Developing an enhanced understanding of mechanical behavior in materials relies upon sufficiently characterizing microstructure details at the relevant length scales that contribute to this behavior. Moreover, to truly enhance the predictive capability of processing-structure-property models that aim to improve material performance requires a quantitative description of the relevant microstructure features and, thereby, the material itself.

301

In this work, we focus on single crystal nickel-based superalloys, which are used in turbine blades within the high temperature section of the modern turbine engine (Reed, 2006). In single crystal nickel-based superalloys, there are a number of length scales of microstructure that contribute to mechanical behavior, ranging from the primary, secondary, and tertiary gamma prime precipitates to pores and eutectic particles to the dendrites themselves. As the dendritic microstructure lies at the largest length scales, it is important to characterize their spacing, as historically the PDAS (primary dendrite arm spacing) has been found to correlate with processing (e.g., solidification rate) (Wang et al., 2003; Brundidge, 2011) as well as with properties (e.g., creep strength, fatigue properties)(Wilson et al., 2008; Lamm and Singer, 2007). Characterizing the spacing of primary dendrite arms in directionally-solidified microstructures is an important step for developing process-structure-property relationships by enabling the quantification of (i) the influence of processing on microstructure and (ii) the influence of microstructure on properties.

The traditional approach for measuring primary dendrite arm spacing in single crystal metals, whereby the number of dendrite cores in a specified area is related to the dendrite arm spacing (Flemings, 1974; Jacobi and Schwerdtfeger, 1976; Warnken and Reed, 2010a, Warnken and Reed 2010b):

$$\lambda = c\sqrt{A/n} \tag{1}$$

where λ is primary dendrite arm spacing, A is the area analyzed, n is the number of dendrites, and c is a coefficient that depends on the microstructure - is insufficient for capturing local arm spacings or the dendrite arm spacing distribution, and may provide problems with complex geometries such as turbine blades.

The research objective herein is to evaluate the capability of various conventional approaches, as well as new or modified approaches, for spatial point pattern analysis with application to characterizing experimental dendritic microstructures. Both computer-generated and experimental dendritic microstructures are used for this analysis along with numerous techniques based on the nearest neighbor spacing, Voronoi tessellation, Delaunay triangulation, or graph theory. Comparison of new metrics with traditional primary dendrite arm spacing metrics will also be discussed for both local and global measures. The current methods investigated will supply information of local spacing and coordination number while addressing edge effects, parameter sensitivity, and correlation with interdendritic features, thus providing insight into how processing affects properties.

302

Methodology

The approach utilized in this work to measure the local dendrite arm spacing is based on a Voronoi tessellation of the spatial array of dendrite cores. To illustrate how the present method works and differs from some other published methods, we generated a synthetic 5x5 cubic pattern of points with a small degree of noise (100% noise fraction, $0.20a_0$ noise fraction [2]), as shown in Figure 1a. For the purposes of describing several different methods shown in Figure 1, this synthetic pattern of points can be considered as the cores of primary dendrites.

One such method for measuring the local dendrite arm spacing is the Warnken-Reed method (Warnken and Reed, 2011). The Warnken-Reed method calculates the dendrite arm spacing for a single point (black dot) by starting with an initial number of nearest neighbors (3 closest neighbors) and iteratively adding potential nearest neighbors that are within a cutoff distance defined by the already-added nearest neighbors. For instance, the inner circle in Figure 1b represents the average spacing, d_{ave}, of these neighbors and the outer circle represents the cutoff for adding the next neighbor, $d_{ave} +\alpha*d_{std}$. Neighbors continue to be added until the cutoff does not include any new neighbors. The local coordination number and dendrite arm spacing is calculated from the neighbors added (shown as red dots). However, if the standard deviation of the distances of the nearest neighbors is large, this technique can continue to add nearest neighbors beyond the first nearest neighbors. Clearly, a method for restricting the number of nearest neighbors using such a technique is necessary.

A simple way of identifying the potential first nearest neighbors is to perform a Voronoi tessellation of the space surrounding the points, as shown in Figure 1c. For the Voronoi tessellation plot, each polygon contains a point and any point placed within a polygon will be closest to the point contained within that polygon. The polygon edges are equidistant between the points contained in the two adjacent polygons and the triple points (merging of three lines) are equidistant between the points contained in the three adjacent polygons. Therefore, the first nearest neighbors (open circles in Fig. 1c) correspond to the edges of the central polygon (that contains the black dot). This subset of points is the maximum number of nearest neighbors that the central point can have.

In this manner, the several techniques can be modified to only include the first nearest neighbors. For instance, the modified Warnken-Reed method (Fig. 1d) only includes these as potential nearest neighbors and cannot expand beyond these, alleviating a potential problem. Another method using these is to consider all of these potential nearest neighbors as nearest neighbors (Fig. 1e). Unfortunately, this approach is sensitive to small perturbations in the spatial positions of the neighbors. For instance, if the lower right hand neighbor in Fig. 1e moves away from the

303

15

central point, it will no longer share an edge with the polygon containing the black dot; in this scenario, the two adjacent polygons on either side will "pinch" off this neighbor. This scenario, however, has a physical basis as these two dendrite cores will mainly compete with the central core, and the lower right core has a much less prominent effect on the central core. The last method, which will be examined in the present paper, utilizes a criterion based on the edge lengths of the Voronoi polygon. In Figure 1f, those neighbors with edge lengths less than a critical fraction of the total polygon perimeter are excluded as nearest neighbors (e.g., 10% in Fig. 1f). In the present study, we consider only this technique in evaluating the local dendrite arm spacing statistics.
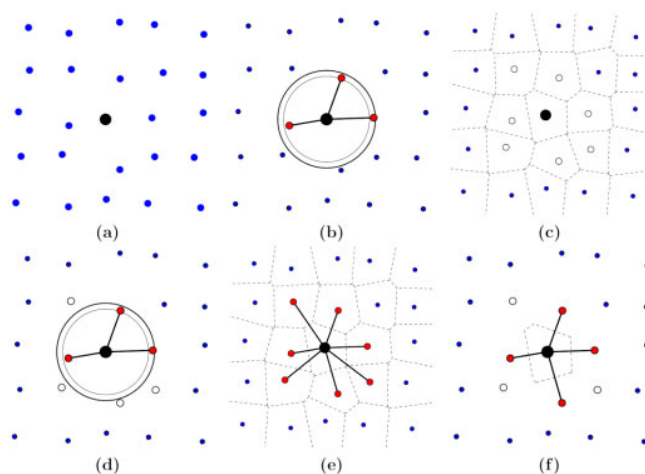

Figure 1. The difference between various methods for defining the nearest neighbors (red dots) and their spacing for a single point (large black dot). (a) Initial 5 x 5 cubic pattern with noise fraction of 100% and noise level of $0.20a_0$. (b) The Warnken-Reed method with $\alpha = 1.5$ and $k_{initial} = 3$. The inner circle represents the average spacing, d_{ave}, of these neighbors and the outer circle represents the cutoff for adding the next neighbor, $d_{ave} + \alpha*d_{std}$. (c) Voronoi tesselation diagram for the points. The potential first nearest neighbors are identified through shared vertices with each point. (d) The modified Warnken-Reed method with $\alpha = 1.5$ and $k_{initial} = 3$, whereby the neighbors are restricted to only those identified using the Voronoi tesselation (further explanation of the difference between (b) and (d) is given in Fig. 6). (e) Using only shared vertices (and connecting lines forming a polygon) to identify the nearest neighbors. (f) Modified tesselation-based technique whereby the nearest neighbors are identified as those with line lengths above a critical threshold fraction of the total perimeter line length d_{crit} of the tesselated polygon for the point.

Results

A micrograph of a directionally-solidified single crystal nickel-based superalloy microstructure that is polished and imaged perpendicular to the solidification direction is shown in Figure 2. This microstructure was produced using the liquid metal cooling technique, as described in

304

Miller (2011) and Elliot et al. (2004). The black dots were manually placed to identify the dendrite cores. Automated methods to identify dendrite cores and other microstructure features have been previously developed and are invaluable to large scale analysis (Tschopp et al., 2010a, 2010b, 2010c, 2010d). The white particles in this image are eutectic particles. A total of 393 dendrite cores are contained in this image over an area of 24.25 mm^2 (PDAS of 248.4 μm). The remainder of the analysis will use this micrograph as a template for characterizing the local dendrite arm spacing.

Figure 2. Dendritic structure normal to the withdrawal direction in a directionally-solidified single crystal nickel-based superalloy cast using the liquid metal cooling technique (Miller, 2010). The dots denote the dendrite cores.

<u>Edge Detection and Metrics</u>

The ability to handle edge effects when computing local dendrite arm spacings with dendrite cores is vital for quantifying statistics in thin sections, such as the wall of an airfoil blade that may only contain 1-3 dendrite cores across the section. As a first example of one such a technique, we have used a convex hull of the dendrite cores in Figure 2 to identify "edge" dendrite cores and quantify the dendrite arm spacing. First, a convex hull is generated around the points; this is the minimum "convex" area that contains all the points and is denoted by a blue dotted line in Figure 3. Next, the edge points are identified by finding those points with vertices that lie outside of the convex hull (white dots). Then, for these points, a new polygon is generated by the intersection of the initial polygon from the Voronoi tessellation and the convex hull (red polygon). Last, the neighbors can now be calculated using either a new criterion or the same criterion used for interior points. For the present analysis, the same criterion (polygon with edge length threshold) was used for all points. Further techniques are needed to deal with

305

17

complex geometries that include concave character and internal passages in order to apply these techniques to turbine blades.
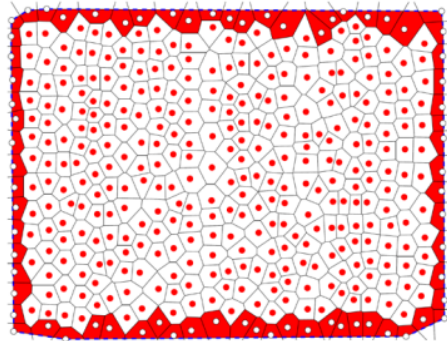

Figure 3. Voronoi tessellation of dendritic structure from Figure 2. The dotted blue line denotes the convex hull of the dendrite cores and the red polygons are those cores that intersect the convex hull.

<u>Comparison of Local Metrics</u>

The local dendrite arm spacing statistics are calculated for both the interior and exterior points to compare with the traditional PDAS measurement. The cumulative distribution plot for the local dendrite arm spacing is shown in Figure 4 and the mean dendrite arm spacing is shown for both sites. First, the interior sites have a mean dendrite arm spacing of 253.3 μm, which is only 2% larger than the bulk-measured 248.4 μm. Moreover, the interior dendrite arm spacings are approximately normally distributed (kurtosis of 2.98 and skewness of 0.21 – a normal distribution has a kurtosis of 3 and a skewness of 0). On the other hand, the exterior sites have a mean dendrite arm spacing of 267.2 μm (~5.5% greater than interior sites) and deviate slightly from normality (kurtosis of 4.49 and skewness of 0.47). This technique allows us to compare measurements for bulk dendrite cores with edge dendrite cores as well as measuring the dendrite arm spacing distribution statistics, which may be important for correlating with both processing and properties.

<u>Local Dendrite Metrics</u>

The spatial distribution of local dendrite arm spacing and coordination number can provide insight into the order/disorder of primary dendrites and can identify regions that could potentially contain more/less interdendritic features and/or contain different properties. For instance, the dendrite arm spacing and coordination number for the directionally-solidified superalloy micrograph (Fig. 2) is shown in Figure 5. Dendrite cores with local PDAS similar to the mean PDAS are colored white and those with PDAS above (below) the mean PDAS are red (blue). In

306

18

general, the exterior dendrite cores have similar PDAS as the interior dendrite cores. A similar colorbar is used for the coordination number as well. As expected, the exterior dendrite cores have a lower coordination number than interior dendrite cores, with a few that only have 2 nearest neighbors. However, the low coordination number dendrite cores on the edge are not consistently over/under the mean PDAS (i.e., they do not significantly bias the statistics from the edge dendrite cores).

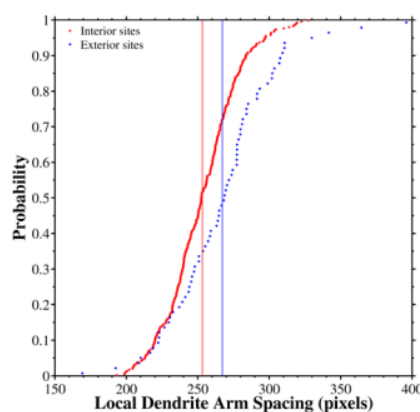**Figure 4.** The cumulative distribution plot of the primary dendrite arm spacings for both interior and exterior dendrite cores in Figure 2. The solid lines represent the mean dendrite arm spacings, which can be compared to the bulk measurement of 248.4 μm.
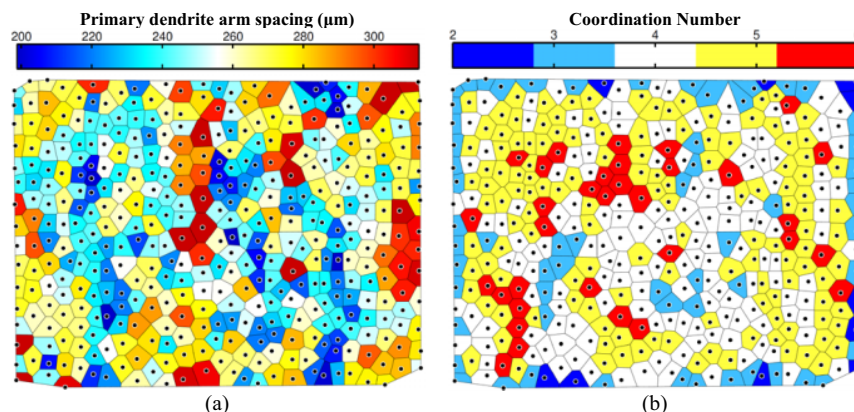

Figure 5. (a) Local dendrite arm spacing (μm) and (b) coordination number based on the Voronoi tessellation with edge length threshold of 10%.

307

19

<u>Correlation with Interdendritic Features</u>

The eutectic particles in Figure 2 were segmented to examine how the occurrence of interdendritic features (e.g., pores or eutectic particles) correlates with local dendrite arm spacing metrics. The particles were segmented by first leveling the intensity of the micrograph using a cubic polynomial with interaction terms and then selecting a threshold to identify the eutectic particles. Following this step, the Euclidean distance to the nearest dendrite core and the nearest Voronoi vertex was calculated for each pixel within the micrograph. The probability of a eutectic particle can then be calculated as a function of this distance, as shown in Figure 6. Based on the image segmentation, the area fraction of eutectic particles in Figure 2 is 3.6% and is shown in red. As can be seen from Fig. 6a, at a distance of approximately 100 microns, the probability of a eutectic particle exceeds the global area fraction, i.e., it is more favorable for a eutectic particle to form. Moreover, this plot shows that it is not favorable for eutectic particles to form close to the primary dendrite core. Figure 6b is a similar plot as a function of distance from the vertices of the Voronoi tessellation. There is an increased occurrence of eutectic particles at vertices, regardless of their distance from the dendrite core. While this analysis shows the preferential formation of eutectic particles based on the local distances, correlation with the size of particles is also important; we leave this for future work.

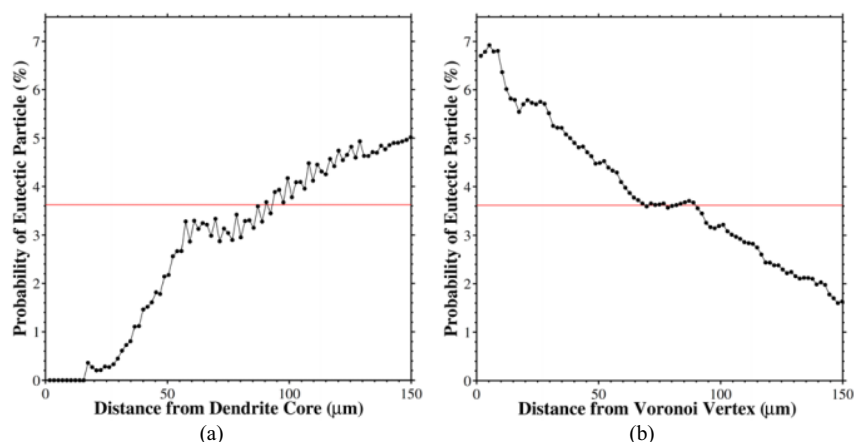(a)   (b)

Figure 6. The probability of a eutectic particle as a function of the distance to (a) the nearest dendrite core or (b) the nearest Voronoi vertex.

Conclusions

Characterizing the spacing of primary dendrite arms in directionally-solidified microstructures is an important step for developing process-structure-property relationships by enabling the

308

quantification of (i) the influence of processing on microstructure and (ii) the influence of microstructure on properties. Thin-walled directionally-solidified structures (e.g., a turbine blade) require new approaches for characterizing the dendrite arm spacing and the microstructure. In this work, we utilized a new approach for spatial point pattern analysis that was applied to an experimental dendritic microstructure. This technique utilizes a Voronoi tessellation of space surrounding the dendrite cores to determine nearest neighbors and the local dendrite arm spacing. Moreover, a convex hull-based technique was used to include edge effects, which can be important for thin specimens. These methods were used to quantify the distribution of dendrite arm spacings and their spatial distribution of dendrite arm spacings through the directionally-solidified superalloy micrograph. Last, the distances from dendrite cores and Voronoi vertices were correlated with the presence of eutectic particles, which can be important for correlating structure to mechanical properties for superalloys.

References

Brundidge, C.L., Miller, J.D., Pollock, T.M., 2011. Development of dendritic structure in the liquid-metal-cooled, directional-solidification process. Metallurgical and Materials Transactions A: Physical Metallurgy and Materials Science 42, 2723–2732.

Elliott, A., Pollock, T., Tin, S., King, W., Huang, S.-C., Gigliotti, M., 2004. Directional solidification of large superalloy castings with radiation and liquid-metal cooling: A comparative assessment. Metallurgical and Materials Transactions A 35, 3221–3231.

Flemings, M., 1974. Solidification processing. Metallurgical and Materials Transactions B 5, 2121–2134.

Jacobi, H., Schwerdtfeger, K., 1976. Dendrite morphology of steady state unidirectionally solidified steel. Metallurgical Transactions A 7, 811–820.

Lamm, M., Singer, R.F., 2007. The Effect of Casting Conditions on the High-Cycle Fatigue Properties of the Single-Crystal Nickel-Base Superalloy PWA 1483. Metallurgical and Materials Transactions A 38, 1177–1183.

Miller, J.D., 2011. Heat Extraction and Dendritic Growth during Directional Solidification of Single-Crystal Nickel-base Superalloys.

Reed, R.C., 2006. The superalloys: fundamentals and applications. Cambridge University Press.

309

Tschopp, M.A., Groeber, M.A., Fahringer, R., Simmons, J.P., Rosenberger, A.H., Woodward, C., 2010a. Symmetry-based automated extraction of microstructural features: Application to dendritic cores in single-crystal Ni-based superalloys. Scripta Materialia 62, 357–360.

Tschopp, M.A., Groeber, M.A., Simmons, J.P., Rosenberger, A.H., Woodward, C., 2010b. Automated extraction of symmetric microstructure features in serial sectioning images. Materials Characterization 61, 1406–1417.

Tschopp, M.A., Tiley, J.S., Viswanathan, G.B., 2010c. Automated Identification and Characterization of Secondary & Tertiary γ' Precipitates in Nickel-based Superalloys. Materials Science & Technology 26(12), 1414-1422.

Tschopp, M.A., Groeber, M.A., Fahringer, R., Simmons, J., Rosenberger, A.H., Woodward, C., 2010d. Automated Detection and 3D Characterization of Microstructural Features: Application to Eutectic Particles in Single Crystal Ni-Based Superalloys. Modelling and Simulation in Materials Science & Engineering 18, 025014.

Wang, W., Lee, P.D., McLean, M., 2003. A model of solidification microstructures in nickel-based superalloys: predicting primary dendrite spacing selection. Acta Materialia 51, 2971–2987.

Warnken, N., Reed, R.C., 2011a. On the characterization of directionally solidified dendritic microstructures. Metallurgical and Materials Transactions A: Physical Metallurgy and Materials Science 42, 1675–1683.

Warnken, N., Reed, R.C., 2011b. A novel method for the characterisation of directionally solidified dendritic arrays, in: IOP Conference Series: Materials Science and Engineering.

Wilson, B.C., Cutler, E.R., Fuchs, G.E., 2008. Effect of solidification parameters on the microstructures and properties of CMSX-10. Materials Science and Engineering: A 479, 356–364.

310

3 Metallurgical and Materials Transactions A Paper, January 2014

This paper was selected as an Editor's Choice as having special significance.

M.A. Tschopp, J.D. Miller, A.L. Oppedal, K.N. Solanki, Characterizing the Local Primary Dendrite Arm Spacing in Directionally Solidified Dendritic Microstructures, Metallurgical and Materials Transactions A. 45 (2014) 426–437.

Characterizing the Local Primary Dendrite Arm Spacing in Directionally Solidified Dendritic Microstructures

MARK A. TSCHOPP, JON D. MILLER, ANDREW L. OPPEDAL, and KIRAN N. SOLANKI

Characterizing the spacing of primary dendrite arms in directionally solidified microstructures is an important step for developing process–structure–property relationships by enabling the quantification of (i) the influence of processing on microstructure and (ii) the influence of microstructure on properties. In this work, we utilized a new Voronoi-based approach for spatial point pattern analysis that was applied to an experimental dendritic microstructure. This technique utilizes a Voronoi tessellation of space surrounding the dendrite cores to determine nearest neighbors and the local primary dendrite arm spacing. In addition, we compared this technique to a recent distance-based technique and a modification to this using Voronoi tessellations. Moreover, a convex hull-based technique was used to include edge effects for such techniques, which can be important for thin specimens. These methods were used to quantify the distribution of local primary dendrite arm spacings, their spatial distribution, and their correlation with interdendritic eutectic particles for an experimental directionally solidified Ni-based superalloy micrograph. This can be an important step for correlating processing and properties in directionally solidified dendritic microstructures.

I. INTRODUCTION

DEVELOPING an enhanced understanding of mechanical behavior in materials relies upon sufficiently characterizing microstructure details at the relevant length scales that contribute to this behavior. Moreover, to truly enhance the predictive capability of processing–structure–property models that aim to improve material performance requires a quantitative stereological description of the relevant microstructure features and, thereby, the material itself. Predictive models that effectively capture the linkage between processing and properties (through microstructure) can be utilized within an integrated computational materials engineering (ICME) approach to design materials and accelerate their insertion into application.

The focus of the present work is on single-crystal nickel-based superalloys, which are used in turbine blades within the high temperature section of the modern turbine engine.[1,2] In single-crystal nickel-based superalloys, there are a number of length scales of microstructure that contribute to mechanical behavior, ranging from the γ' precipitates to pores and eutectic particles to the dendrites themselves. At the largest microstructure length scale in directionally solidified single-crystal microstructures, the features of interest are the dendrites; many features at lower length scales (e.g., eutectic particles, precipitates, etc.) or at similar scales (e.g., porosity, freckle defects, etc.) are strongly associated with the dendrite arm spacing and morphology.[3–7] The solidification morphology associated with dendrite arm spacing has been described in the literature.[8,9] Historically, the primary dendrite arm spacing (PDAS) has been found to correlate with processing (e.g., solidification rate)[7,10–14] as well as with properties (e.g., creep strength, fatigue properties).[15,6] For instance, Lamm and Singer[6] produced single-crystal nickel-based microstructures (PWA 1483) with a varied range of different dendrite arm spacings (250 to 600 μm) and found that decreasing the mean dendrite arm spacing was associated with an increased high-cycle fatigue life. The fatigue cracks were found to originate at shrinkage porosity and the largest pores correlated with a large PDAS.

The traditional approach for measuring PDAS in single-crystal metals, whereby the number of dendrite cores in a specified area is related to the dendrite arm spacing[10,16,17] is given by:

$$\lambda = c\sqrt{\frac{A}{n}}, \qquad [1]$$

where λ is PDAS, A is the area analyzed, n is the number of dendrites, and c is a coefficient that depends on the microstructure. McCartney and Hunt[10] showed that $c = 0.5$ for a random array of points, $c = 1$ for a

MARK A. TSCHOPP, Senior Research Scientist, is with the Lightweight and Specialty Metals Branch, Materials and Manufacturing Science Division, Army Research Laboratory, Aberdeen Proving Ground, MD 21005, and also with the Center for Advanced Vehicular Systems, Mississippi State University, Starkville, MS 39759. Contact e-mail: mark.a.tschopp.ctr@mail.mil JON D. MILLER, Senior Materials Research Engineer, is with the Air Force Research Laboratory, Wright-Patterson AFB, Dayton, OH 45433. ANDREW L. OPPEDAL, Postdoctoral Associate, is with the Center for Advanced Vehicular Systems, Mississippi State University. KIRAN N. SOLANKI, Assistant Professor, is with the School for Engineering of Matter, Transport, and Energy, Arizona State University, Tempe, AZ 85287.
Manuscript submitted June 14, 2013.
Article published online September 17, 2013.

square array of points, and $c = 1.075$ for a hexagonal array of points; they had to apply a correction for the bulk dendrite arm spacing λ as processing conditions caused a change in the local environment of the dendrites. However, this approach is insufficient for capturing local arm spacings or the dendrite arm spacing distribution, and may provide problems with complex geometries such as turbine blades. In fact, part of the motivation for quantifying the local PDAS is that a narrow distribution (*i.e.*, low standard deviation) of local PDAS values may result in a more homogeneous distribution of interdendritic microstructure features and, more importantly, a narrow distribution of mechanical properties.[18] For instance, structural inhomogeneities in single-crystal components, which may cause wider property variations, have been correlated to asymmetric heat flux and transients in solidifications.[19]

The research objective herein is to evaluate the capability of some recent approaches, as well as some modified versions of these approaches, for characterizing the local dendrite arm spacing within experimental dendritic microstructures. In this work, an experimental dendritic microstructure is used for this analysis along with three different techniques that are based on the nearest neighbor spacing and/or a Voronoi tessellation of the dendrite cores. Comparison of existing and new metrics with traditional PDAS metrics is discussed for both local and global measures. The current methods investigated supply statistical information of local spacing and coordination number while introducing a technique for addressing edge effects and examining the parameter sensitivity of these different methods. In comparison to previous work,[20] this work introduces and compares the statistical distributions of local dendrite arm spacings for the four methods, for a more quantitative analysis. It was found that augmenting existing techniques with Voronoi tessellations to define the subset of first nearest neighbors or refining existing Voronoi-based techniques resulted in a more physical description of the local dendrite arm spacing. Moreover, for certain cases, the mean local dendrite statistics can adequately approximate the PDAS found with the traditional bulk characterization technique (Eq. [1]).

II. METHODOLOGY

The approach utilized herein to measure the local dendrite arm spacing is based on a Voronoi tessellation of the spatial array of dendrite cores. The following analysis techniques were implemented in MATLAB R2012a (The MathWorks, Inc.). To illustrate how the present method works and differs from some other published methods, we generated a synthetic 5×5 cubic pattern of points with a small degree of noise (100 pct noise fraction, $0.20a_0$ noise fraction[2]), as shown in Figure 1(a).[20] For the purposes of describing several different methods shown in Figure 1, this synthetic pattern of points can be considered as the cores of primary dendrites.

One such method for measuring the local dendrite arm spacing is the Warnken–Reed method.[21,22] The Warnken–Reed method calculates the dendrite arm spacing for a single point (black dot) by starting with an initial number of nearest neighbors, $k_{initial}$, (3 closest neighbors) and iteratively adding potential nearest neighbors that are within a cutoff distance defined by the already-added nearest neighbors. For instance, the inner circle in Figure 1(b) represents the average spacing, d_{avg}, of these neighbors and the outer circle represents the cutoff for adding the next neighbor, $d_{avg} + \alpha d_{std}$, where d_{std} is the standard deviation of the nearest neighbor spacings and α is a parameter that is typically between 1 and 2. Neighbors continue to be added until the cutoff does not include any new neighbors. The local coordination number and dendrite arm spacing is calculated from the neighbors added (shown as red dots). However, if the standard deviation of the distances of the nearest neighbors d_{std} or the parameter α is large, this technique can continue to add nearest neighbors beyond the first nearest neighbors; our implementation stopped after 20 nearest neighbors. Clearly, a method for restricting the number of nearest neighbors using such a technique is necessary.

A simple way of identifying the potential first nearest neighbors is to perform a Voronoi tessellation of the space surrounding the points, as shown in Figure 1(c). The polygon edges are equidistant between the points contained in the two adjacent polygons and the triple points (merging of three lines) are equidistant between the points contained in the three adjacent polygons. Therefore, the first nearest neighbors (FNNs, shown as open circles in Figure 1(c)) correspond to the edges of the central polygon (that contains the black dot). This subset of points is the maximum number of nearest neighbors that the central point can have.

In this manner, several techniques have been identified to quantify a local dendrite arm spacing based on the Voronoi-identified FNNs.[20] For instance, the Voronoi Warnken–Reed method (Figure 1(d)) only includes the Voronoi FNNs as potential nearest neighbors and cannot expand beyond these, alleviating a potential problem of selecting second nearest neighbors or greater. Another method using the Voronoi FNNs is to consider all of these potential nearest neighbors as nearest neighbors (Figure 1(e)), as in Brundidge *et al.*[14] Unfortunately, this approach is sensitive to small perturbations in the spatial positions of the neighbors. For instance, if the lower right hand neighbor in Figure 1(e) moves away from the central point, it no longer shares an edge with the polygon containing the black dot; in this scenario, the two adjacent polygons on either side effectively "pinch" off this neighbor. This scenario, however, has a physical basis as these two dendrite cores mainly compete with the central core, and the lower right core has a much less prominent effect on the central core. The last method, which is examined in the present paper, utilizes a criterion based on the edge lengths of the Voronoi polygon. In Figure 1(f), those neighbors with edge lengths less than a critical fraction, d_{crit}, of the total polygon perimeter are excluded as nearest neighbors (*e.g.*, 10 pct in Figure 1(f)). In the present study, the local dendrite arm spacing statistics are evaluated using these four techniques:
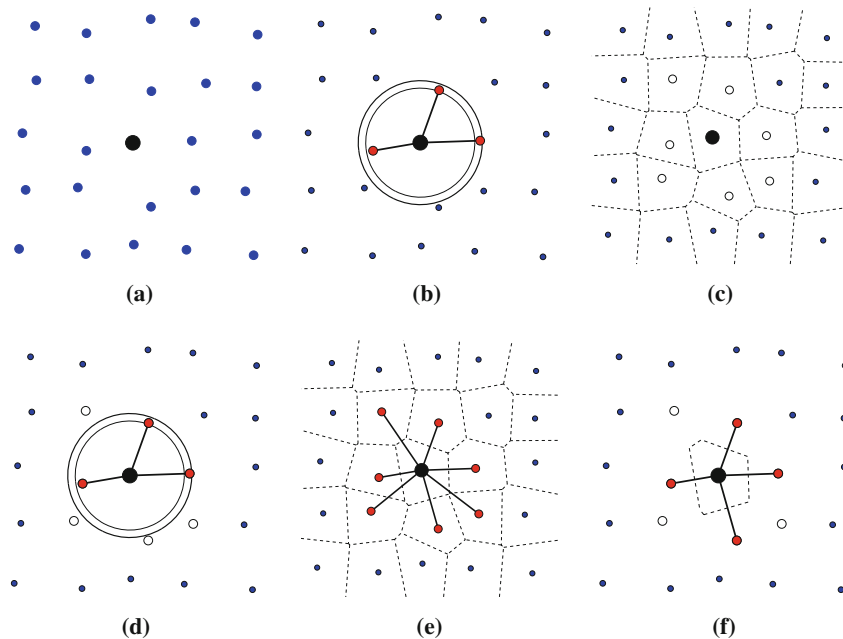
Fig. 1—The difference between various methods for defining the nearest neighbors (red dots) and their spacing for a single point (large black dot). (a) Initial 5 × 5 cubic pattern with noise fraction of 100 pct and noise level of $0.20a_0$. (b) The Warnken–Reed method with $\alpha = 1.5$ and $k_{\text{initial}} = 3$. The inner circle represents the average spacing, d_{avg}, of these neighbors and the outer circle represents the cutoff for adding the next neighbor, $d_{\text{avg}} + \alpha d_{\text{std}}$. (c) Voronoi tessellation diagram for the points. The potential first nearest neighbors are identified through shared vertices with each point. (d) The modified Warnken–Reed method with $\alpha = 1.5$ and $k_{\text{initial}} = 3$, whereby the neighbors are restricted to only those identified using the Voronoi tessellation. (e) Using only shared vertices (and connecting lines forming a polygon) of the Voronoi tessellation to identify the nearest neighbors ($d_{\text{crit}} = 0.0$). (f) Modified tessellation-based technique whereby the nearest neighbors are identified as those with line lengths above a critical threshold fraction of the total perimeter line length $d_{\text{crit}} = 0.10$ of the tessellated polygon for the point (Reprinted from[20]) (Color figure online).

Warnken–Reed, Voronoi Warnken–Reed, and the Voronoi technique with ($d_{\text{crit}} > 0$) and without ($d_{\text{crit}} = 0$) a line length threshold.

As an example of a more disordered structure, Figure 2 plots the four different methods for a different configuration of surrounding points (dendrite cores). In Figure 2(b), the iterative Warnken–Reed method continues to non-physically add neighbors beyond the first nearest neighbors due to a large initial d_{std} value from the initial three distances. The Voronoi-modified version in Figure 2(d) stops at four nearest neighbors despite the fact that several points lie within the outer boundary computed by this method. The Voronoi method with $d_{\text{crit}} = 0.0$ clearly overestimates the number of nearest neighbors, while the four nearest neighbors identified through $d_{\text{crit}} = 0.10$ (Figure 2(f)) perhaps offers a better approximation of the number of nearest neighbors. Interestingly, comparing the methods in Figures 2(d) and (f), the coordination number is the same, but the nearest neighbors identified is different. This is due to the Warnken–Reed method being a distance-based method, and identifying the four closest neighbors, while the modified Voronoi technique is based on the edge lengths of the Voronoi polygon, and hence utilizes

this to identify nearest neighbors (which may not be the closest neighbors).

The traditional PDAS metric does not consider the order or disorder of the dendrites within the microstructure. Figure 2 illustrates why a local metric for PDAS may be needed. For the field of view given in Figures 1(a) and 2(a), the bulk PDAS metric would be the same since the number of dendrites n and the area A are equal (see Eq. [1]). However, the disorder of the dendritic structure in the case of Figure 2 may yield (i) a more uneven distribution of solute elements, (ii) the formation of second phase particles, (iii) the formation of gas or shrinkage porosity, or (iv) the lateral growth of secondary dendrite arms. Hence, in addition to the bulk PDAS values, understanding how processing conditions may impact the disorder of the dendritic structure may be important for understanding the properties of directionally solidified alloys.

Other techniques exist for quantifying the homogeneity or heterogeneity of PDAS in directionally solidified dendritic microstructures. For instance, the minimal spanning tree (MST) method[23] provides a statistical analysis of the disorder in a system of points by connecting all points with the shortest line segments
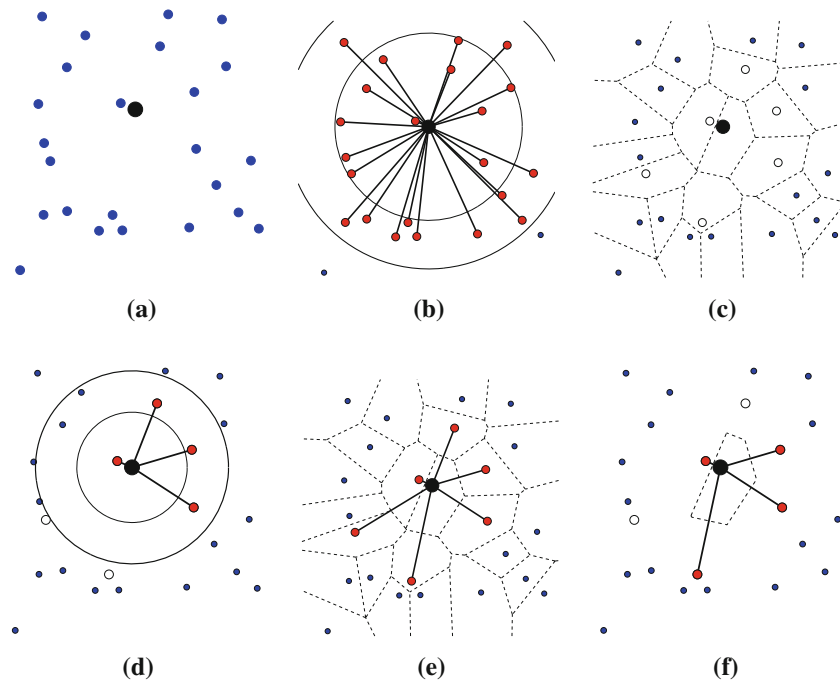
Fig. 2—The difference between various methods for defining the nearest neighbors (red dots) and their spacing for a single point (large black dot) with a distorted local environment. Parts (*a*) through (*f*) are as Fig. 1: (a) initial pattern, (b) the Warnken–Reed method with $\alpha = 1.5$ and $k_{\text{initial}} = 3$, (c) the Voronoi tessellation diagram for the points, (d) the Voronoi-modified Warnken–Reed method with $\alpha = 1.5$ and $k_{\text{initial}} = 3$, (e) the Voronoi method ($d_{\text{crit}} = 0.0$), and (f) the modified tessellation-based technique with $d_{\text{crit}} = 0.10$ (Color figure online).

possible. In this manner, the mean distance of all line segments (m) and the standard deviation (σ) characterize the disorder of the system and casting these values into a m-σ design space allows for comparison between different point systems.[23] This has been effectively applied to characterize the mean dendrite arm spacing, PDAS distribution, and the disorder in first Pb-Tl alloys[24] and subsequently in other alloy systems.[11,18,25] As an example of this technique, Figure 3 plots the dendrite cores and connecting line segments for the single-crystal nickel-based superalloy micrograph used in this study (Figure 4). Moreover, other methods such as radial distribution functions, fast Fourier transforms, and/or correlation functions can also be used to characterize the dendrite arm spacing distribution. However, it should be noted that these approaches are not intended for local characterization of the dendrite arm spacing and are not as effective for correlating the local spacing with local microstructure features as shown herein. Moreover, these techniques do not quantify the number of nearest neighbors and are often coupled with Voronoi polygons to compute the nearest neighbor distributions. Rather, these analysis methods are more effective at characterizing and comparing the homogeneity/heterogeneity of the dendritic structure between different processing conditions. Hence, there will be limited discussion of these techniques in the present work.

III. RESULTS

A. *Application to Dendritic Microstructure*

A micrograph of a directionally solidified single-crystal nickel-based superalloy microstructure that is polished and imaged perpendicular to the solidification direction is shown in Figure 4. This microstructure was produced using the liquid metal cooling technique, as described in Miller[26] and Elliott *et al.*[4] First, the dendrite cores were identified manually (white and black dots). Automated methods to identify dendrite cores can be invaluable for future large scale analysis.[27,28] Moreover, the white particles in this image are eutectic particles. A total of 393 dendrite cores are contained in this image over an area of 24.25 mm^2, giving a PDAS of 248.4 μm using $c = 1$ (Eq. [1]). The remainder of the analysis uses this micrograph as a template for characterizing the local dendrite arm spacing.

B. *Accounting for Image/Part Edge Effects*

The ability to handle edge effects when computing local dendrite arm spacings with dendrite cores is vital for quantifying statistics in thin sections, such as the wall of an airfoil blade that may only contain 1 to 3 dendrite cores across the section.[27,28] As a first example of one such a technique, we have used a convex hull of
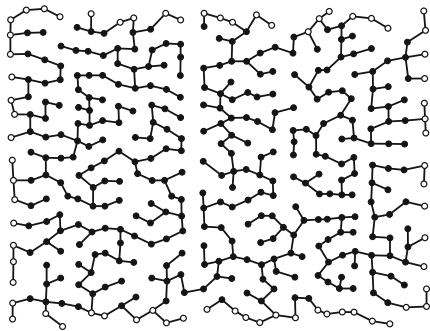
Fig. 3—Minimal spanning tree method[23] for defining the spacing and homogeneity of a microstructure (set of points), whereby the lines represent the minimal distance of connecting line segments. The set of points selected for this example were selected from the dendrite cores shown in Fig. 4, where the white dots indicate 'edge' dendrite cores.
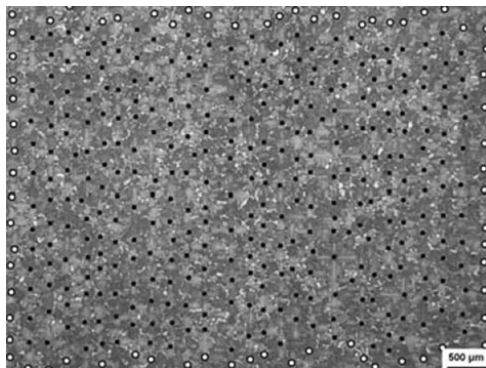

Fig. 4—Dendritic structure normal to the withdrawal direction in a directionally solidified single-crystal nickel-based superalloy cast using the liquid metal cooling technique.[26] The dots denote the dendrite cores, where the white dots indicate 'edge' dendrite cores, as discussed in Fig. 5 and the associated text.

the dendrite cores in Figure 4 to identify "edge" dendrite cores and quantify the dendrite arm spacing. The dendrite core locations are first extracted from the experimental image, as shown in Figure 5. Then, a convex hull is generated around the points; this is the minimum "convex" area that contains all the points. Next, the edge points (white dots in Figure 4) are identified by finding those points with Voronoi vertices that lie outside of the convex hull (dotted blue line in Figure 5(a)). Then, to utilize Voronoi-based techniques for these points, a new polygon is generated by the intersection of the initial polygon from the Voronoi tessellation and the convex hull; the new polygon of the edge dendrite cores is colored red in Figure 5(a) to distinguish from the bulk dendrite cores. The polygons belonging to the interior and edge dendrites are shown in Figures 5(b) and (c), with a random coloring scheme

(a) Convex hull

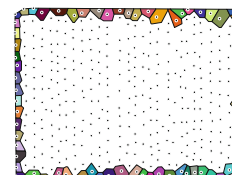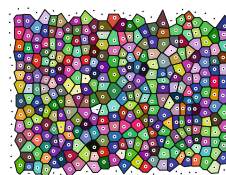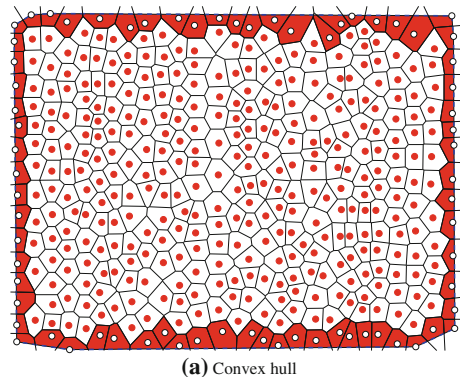**(b)** Interior dendrite cores   **(c)** Edge dendrite cores

Fig. 5—(a) Voronoi tessellation of dendritic structure from Fig. 4. The dotted blue line (surrounding the points) denotes the convex hull of the dendrite cores and the red polygons delineate the cores that intersect the convex hull. The interior and edge dendrites are shown in (b) and (c), respectively, with each polygon colored differently as a guide to the eye (Color figure online).

used to delineate the different polygons. Last, the neighbors can now be calculated using either a new criterion or the same criterion used for interior points. For the present analysis, the same criterion (polygon with edge length threshold) was used for all points; although herein the interior dendrite cores are used to compare statistics with other techniques and bulk PDAS values. More complicated techniques are needed to deal with complex geometries that include concave character and internal passages in order to eventually apply these techniques to complex structures such as turbine blades. Multiple instantiations of microstructures with edge effects can shed light on the appropriate method for determining the local PDAS at edges, which may be different from that used in the interior.

C. Spatial Distribution of Local Primary Dendrite Arm Spacings

The spatial distribution of local dendrite arm spacing and coordination number can provide insight into the order/disorder of primary dendrites and can identify regions that could potentially contain more/less interdendritic features and/or contain different properties. For instance, the PDAS and coordination number for the directionally solidified superalloy micrograph (Figure 4) is shown in Figure 6. In this example, we used the Voronoi tessellation-based technique with an edge length threshold of $d_{crit} = 0.12$. Dendrite cores with local

PDAS similar to the mean PDAS of the bulk (248.4 μm) are colored white and those with PDAS above (below) the mean PDAS are red (blue); the lower and upper bounds of the color bar are -25 and $+25$ pct of the mean PDAS value, respectively. In general, the exterior den-
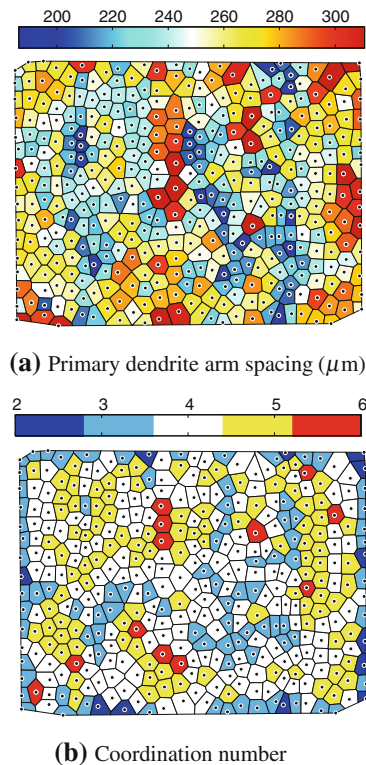

(a) Primary dendrite arm spacing (μm)

(b) Coordination number

Fig. 6—(a) Local dendrite arm spacing (μm) and (b) coordination number based on the Voronoi tessellation with edge length threshold of $d_{crit} = 0.12$ or 12 pct.

drite cores have similar PDAS as the interior dendrite cores using this technique. A similar color bar is used for the coordination number as well. As would be expected, the exterior dendrite cores tend to have a lower coordination number than the interior dendrite cores, with a few that only have 2 nearest neighbors. However, the dendrite cores with a low coordination number on the edges are not consistently over/under the mean PDAS (*i.e.*, they do not significantly bias the statistics from the edge dendrite cores). Future work will examine what techniques may be most applicable for characterizing local dendrite arm spacings and coordination numbers for dendrite cores on free surfaces. It is envisioned that sectioning large numbers of instantiations of syntheti-cally generated microstructures of known bulk dendrite arm spacings can be used to understand the bias introduced by edge effects and to understand what are the best techniques for quantifying the local spacing.

The local dendrite arm spacing for the remaining three techniques is shown in Figure 7. The same color bar for local PDAS as in Figure 6 is used here. First, notice that the Voronoi tessellation-based technique with an edge length threshold of $d_{crit} = 0.0$ has a much larger fraction of dendrite cores with PDAS greater than the bulk PDAS than below the bulk PDAS (83.5 pct above 248.4 μm). Clearly, the local PDAS is overpredicted in this case. The Warnken–Reed and Voronoi Warnken–Reed methods are shown in Figures 7(b) and (c). At first glance, a majority of the local PDAS values are very similar between the two methods (~79 pct). However, ~21 pct of the cores resulted in a difference between the two techniques, which is caused by the original Warnken–Reed method using neighbors outside of those FNNs identified from the Voronoi polygons. In every case, the Warnken–Reed method resulted in higher local PDAS values than the Voronoi Warnken–Reed method, as would be expected since this is purely a distance-based method and sub-sequent additions can only increase the local PDAS.

Figure 8 shows the difference in local PDAS values between the two techniques. In several cases, the difference is greater than 250 μm and/or 100 pct of the PDAS value quantified by the Voronoi Warnken–Reed method. The differing dendrite cores is approximately

(a) Voronoi Tessellation ($d_{crit} = 0.0$)   **(b)** Warnken-Reed ($\alpha = 2.0$)   **(c)** Voronoi Warnken-Reed ($\alpha = 2.0$)
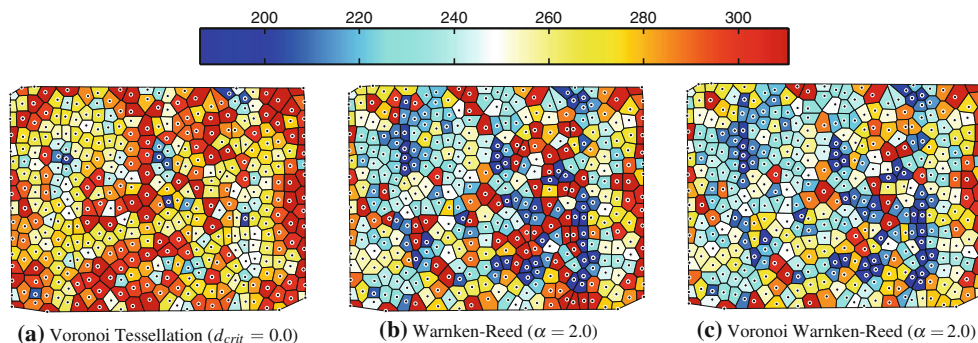
Fig. 7—Local dendrite arm spacing (μm) for the three techniques not shown in Fig. 6: (a) Voronoi tessellation with edge length threshold of $d_{crit} = 0.0$, (b) Warnken–Reed technique with $\alpha = 2.0$, and (c) Voronoi Warnken–Reed with $\alpha = 2.0$.

an equal percentage for edge dendrites as well as interior dendrite cores.

D. *Local Primary Dendrite Arm Spacing Statistics*

The local dendrite arm spacing statistics are also calculated for the interior dendrite cores to compare with the traditional PDAS measurement. The cumulative distribution function plot for the local dendrite arm spacing is shown in Figure 9 for the three different techniques over a range of parameter values, which are
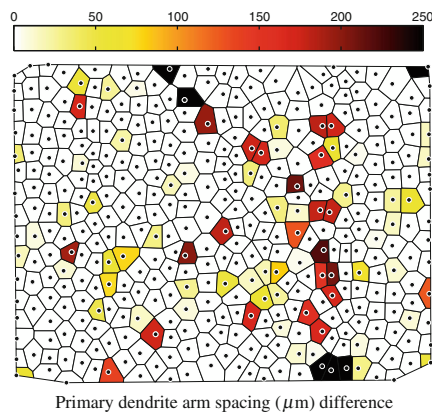
Fig. 8—Difference in the local dendrite arm spacing (μm) between the Warnken–Reed and Voronoi Warnken–Reed techniques with $\alpha = 2.0$. The Warnken–Reed technique had a greater PDAS value in every case (~21 pct of dendrite cores are different).

given in the legend. The bulk PDAS measurement is shown as a vertical black line and the hexagonal star shows the 50th percentile intersection point. The local dendrite arm spacing distributions are characterized in terms of mean, standard deviation, skewness, and kurtosis (Table I), while the coordination number distributions are characterized in terms of their mean and the percentages of 3, 4, 5, 6, and $7+$ nearest neighbors (Table II). The skewness and kurtosis measure the asymmetry of the distribution and the sharpness of the peak/thickness of the tail, respectively. The skewness and kurtosis are 0 and 3, respectively, for a normal distribution.

There are distinct differences between the local dendrite arm spacing distributions calculated by the four techniques (Figure 9 and Table I). The Warnken–Reed and Voronoi Warnken–Reed are compared initially. In the case of the Warnken–Reed method, the PDAS distribution is shifted towards large PDAS values at high α values (a positive skewness value gives a long tail) and has a sharper peak and a longer, fatter tail (high kurtosis values), more so than the other methods. This skewness is caused by an overestimation of the number of nearest neighbors in some cases, due to large values of either d_{std} or the parameter α. For the Voronoi Warnken–Reed method, there is a lack of a long tail and the skewness/kurtosis of the distribution tends more towards normality. However, the calculated mean PDAS with this method tends to underestimate the bulk-measured PDAS. While the maximum number of nearest neighbors (8 for $\alpha \geq 1.2$) is more realistic, a large percentage of dendrite cores are predicted to have only 3 nearest neighbors, even in the case of a large α parameter (48.6 pct for $\alpha = 2.0$). It is also interesting that increasing the α parameter for the case of the
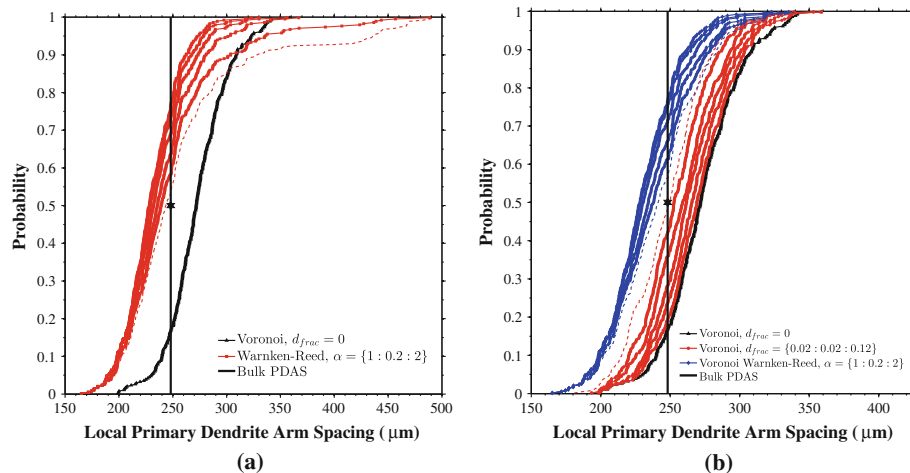
Fig. 9—Probability distribution functions for the various local characterization methods compared within for the internal dendrites within the dendritic microstructure shown in Fig. 4. The four different techniques are compared with the bulk PDAS for a range of parameter values. The upper bound of the parameter range for each technique is shown as a dotted line. To facilitate the comparison, the Warnken–Reed and the Voronoi technique ($d_{crit} = 0.0$) are shown in (*a*), and the remaining Voronoi-modified techniques are shown in (*b*).

Table I. Local Primary Dendrite Arm Spacing Statistics

Method	Parameter	Primary Dendrite Arm Spacing				
		Mean (μm)	Diff. (Pct)	Std (μm)	Skewness	Kurtosis
Bulk (Eq. [1], $c = 1$)	—	248.4	0.0	—	—	—
Voronoi Tessellation	$d_{crit} = 0.00$	272.9	9.9	28.0	0.1	3.3
Voronoi Tessellation	$d_{crit} = 0.02$	270.0	8.7	27.2	0.1	3.2
Voronoi Tessellation	$d_{crit} = 0.04$	266.4	7.2	26.8	0.1	3.1
Voronoi Tessellation	$d_{crit} = 0.06$	263.0	5.9	25.7	0.1	3.1
Voronoi Tessellation	$d_{crit} = 0.08$	258.4	4.0	26.1	0.2	3.1
Voronoi Tessellation	$d_{crit} = 0.10$	253.3	2.0	25.3	0.2	3.0
Voronoi Tessellation	$d_{crit} = 0.12$	247.6	−0.3	26.0	0.2	2.9
Voronoi Warnken–Reed	$\alpha = 1.0$	230.0	−7.4	25.0	0.4	3.5
Voronoi Warnken–Reed	$\alpha = 1.2$	230.9	−7.0	26.0	0.4	3.4
Voronoi Warnken–Reed	$\alpha = 1.4$	232.7	−6.3	27.4	0.4	3.2
Voronoi Warnken–Reed	$\alpha = 1.6$	236.1	−5.0	29.5	0.4	3.1
Voronoi Warnken–Reed	$\alpha = 1.8$	239.0	−3.8	30.5	0.4	3.0
Voronoi Warnken–Reed	$\alpha = 2.0$	242.2	−2.5	31.8	0.3	3.0
Warnken–Reed	$\alpha = 1.0$	230.1	−7.4	25.1	0.3	3.4
Warnken–Reed	$\alpha = 1.2$	231.8	−6.7	26.9	0.5	3.5
Warnken–Reed	$\alpha = 1.4$	234.5	−5.6	29.4	0.6	3.8
Warnken–Reed	$\alpha = 1.6$	239.2	−3.7	33.0	0.8	4.0
Warnken–Reed	$\alpha = 1.8$	248.1	−0.1	48.1	1.9	8.3
Warnken–Reed	$\alpha = 2.0$	259.2	4.3	64.2	1.9	6.5
Minimal Spanning Tree	N/A	215.2	−13.4	34.1	−0.5	4.8

Table II. Local Coordination Number Statistics

Method	Parameter	Coordination Number (Pct)					
		3	4	5	6	≥7	Mean
Voronoi Tessellation	$d_{crit} = 0.00$	0.0	2.5	20.4	57.3	19.8	5.98
Voronoi Tessellation	$d_{crit} = 0.02$	0.0	4.0	26.0	57.0	13.0	5.80
Voronoi Tessellation	$d_{crit} = 0.04$	0.0	7.4	34.7	51.4	6.5	5.57
Voronoi Tessellation	$d_{crit} = 0.06$	0.0	11.8	45.2	39.9	3.1	5.35
Voronoi Tessellation	$d_{crit} = 0.08$	1.5	24.1	49.2	24.8	0.3	4.98
Voronoi Tessellation	$d_{crit} = 0.10$	5.3	43.0	41.5	10.2	0.0	4.57
Voronoi Tessellation	$d_{crit} = 0.12$	17.3	52.3	26.9	3.4	0.0	4.16
Voronoi Warnken–Reed	$\alpha = 1.0$	94.1	4.6	0.9	0.0	0.3	3.08
Voronoi Warnken–Reed	$\alpha = 1.2$	87.6	8.7	2.8	0.3	0.6	3.18
Voronoi Warnken–Reed	$\alpha = 1.4$	79.3	11.8	5.3	2.5	1.2	3.35
Voronoi Warnken–Reed	$\alpha = 1.6$	65.9	18.0	8.0	5.3	2.8	3.62
Voronoi Warnken–Reed	$\alpha = 1.8$	56.3	19.8	12.1	8.4	3.4	3.84
Voronoi Warnken–Reed	$\alpha = 2.0$	48.6	19.8	14.9	11.5	5.3	4.07
Warnken–Reed	$\alpha = 1.0$	91.6	7.1	0.9	0.0	0.3	3.10
Warnken–Reed	$\alpha = 1.2$	83.9	9.6	4.0	1.2	1.2	3.27
Warnken–Reed	$\alpha = 1.4$	72.8	14.6	7.1	2.8	2.8	3.52
Warnken–Reed	$\alpha = 1.6$	58.5	21.7	9.0	4.0	6.8	3.89
Warnken–Reed	$\alpha = 1.8$	52.0	19.2	10.8	6.2	11.8	4.63
Warnken–Reed	$\alpha = 2.0$	44.0	19.2	12.1	7.1	17.6	5.55

Voronoi Warnken–Reed method tends to shift the slope of the probability distribution function without affecting either the minimum or maximum local dendrite arm spacings.

For comparison, the minimal spanning tree method (Figure 3) was also included in Table I. Not surprisingly, the mean distance of the connecting line segments is much shorter than the bulk calculated PDAS using Eq. [1] with $c = 1$. Remember that the MST method is composed of the shortest line segments to connect all dendrites. Both the MST standard deviation and kurtosis values are larger than the Voronoi tessellation method (for all d_{crit}) and the Voronoi Warnken–Reed method (for all α), indicating a wider distribution and a larger deviation of the distribution from normality (kurtosis = 3). Moreover, the distribution is skewed towards a larger tail at lower distances (negative skewness) unlike the other techniques, which again is associated with the selection of the shortest line segments to characterize the spacing.

Quantifying the coordination number and the local PDAS values using all FNNs identified by the Voronoi tessellation polygons ($d_{crit} = 0$) clearly overestimates both measures; mean PDAS is ~10 pct off from the bulk-measured PDAS value and ~20 pct of dendrite cores have more than 6 nearest neighbors. As the edge length threshold parameter increases, less nearest neighbors are identified and the calculated mean PDAS approaches the bulk-measured PDAS value (within 0.3 pct for $d_{crit} = 0.12$). For $d_{crit} = 0.12$, the majority of dendrite cores have 4 nearest neighbors (>50 pct), followed by 5 nearest neighbors (26.9 pct) and 3 nearest neighbors (17.3 pct). Moreover, the local PDAS distribution has a low skewness value (0.2) and a kurtosis of 2.9, indicating an approximately normal distribution. In general, the Voronoi tessellation-based technique with an edge length threshold criterion of $d_{crit} = 0.12$ tends to give the best agreement in terms of both bulk-measured PDAS and coordination number.

E. Correlation with Interdendritic Features

The relationship between the occurrence of interdendritic features (e.g., pores or eutectic particles) and the local dendrite arm spacing (or distance from cores, etc.) can provide insight into the importance of quantifying the local spacings. We have examined how these metrics may relate to the formation of eutectic particles in this work by first segmenting the interdendritic particles and then computing probability distribution functions.

The eutectic particles in Figure 4 were segmented using the following process. The particles were segmented by first leveling the intensity of the micrograph using a cubic polynomial with interaction terms. This step ensured that there was no shift in contrast from one side of the micrograph to the other (due to uneven etching, etc.). The threshold intensity was then selected by maximizing the difference in the mean intensity between the two distributions (eutectic particle and matrix). Then, a size threshold was enforced by discarding eutectic particles with less than 5 pixels (1 pixel ~1.7 μm, i.e., 5 pixels = 15.2 μm^2). As an example of the segmentation, Figure 10(a) shows a 1mm $\times$ 1 mm region from Figures 4 and 10(b) shows the corresponding binary image of the segmented eutectic particles (in white). While other segmentation techniques, such as region growing,[29] have been used to segment these interdendritic particles features in 3D serial slices, the method utilized within produced sufficient segmentation of the particles for the subsequent analysis.

The Euclidean distance to the nearest dendrite core and the nearest Voronoi vertex was then calculated for each pixel within the micrograph. The Euclidean distance is the distance from each pixel to the nearest feature, which in this case is either the centroids of the dendrite cores or the Voronoi vertices, and this metric is repeated over all pixels within the image to create a map. As an example, Figure 10(c) shows the Euclidean distance map for the same 1 mm $\times$ 1 mm area utilizing the dendrite core centroids identified in Figure 4. The darker intensity indicates closer Euclidean distances to the dendrite core and the lightest pixels between the dendrite cores actually correspond to the boundaries of the Voronoi tessellation.

The probability of encountering (or forming) a eutectic particle can then be calculated as a function of this Euclidean distance from the nearest dendrite core or the Voronoi vertex, as shown in Figure 11. Based on the image segmentation, the area fraction of eutectic particles in Figure 4 is 3.6 pct and is shown as a red line in Figure 11. The pixels lying within 100 μm of the image boundaries were excluded to eliminate the possibility that dendrite cores just outside of the image field of view could affect the statistics. As can be seen from Figure 11(a), the left (right) blue line indicates the distance whereby all distances below (above) have a probability of having a eutectic particle that is lower (higher) than the global area fraction (red line), i.e., it is less (more) favorable for a eutectic particle to form. The transition distance of eutectic particle favorability is between 86 and 93 μm, i.e., ~1/3 of the PDAS (248.4 μm). This plot shows that it
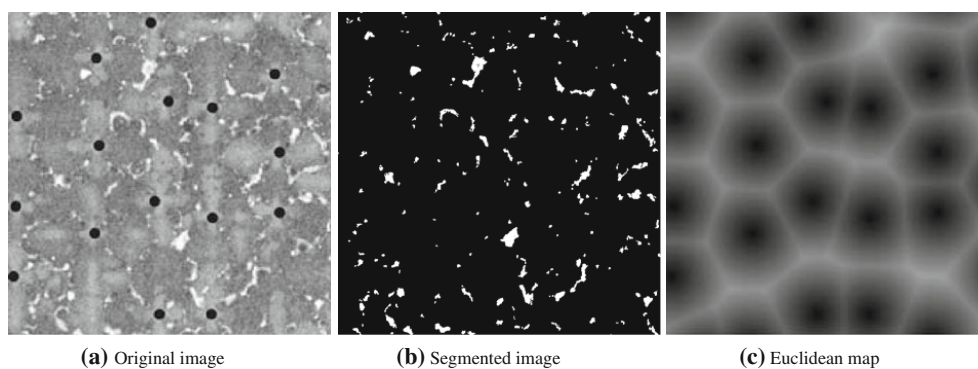

(a) Original image **(b)** Segmented image **(c)** Euclidean map

Fig. 10—(a) A 1 mm $\times$ 1 mm subregion from Fig. 4 is shown along with two corresponding images of the same area: (b) a binary image with segmented eutectic particles (white) and (c) a Euclidean distance map from the dendrite core centroids, where lighter intensity refers to further distances from the dendrite cores.
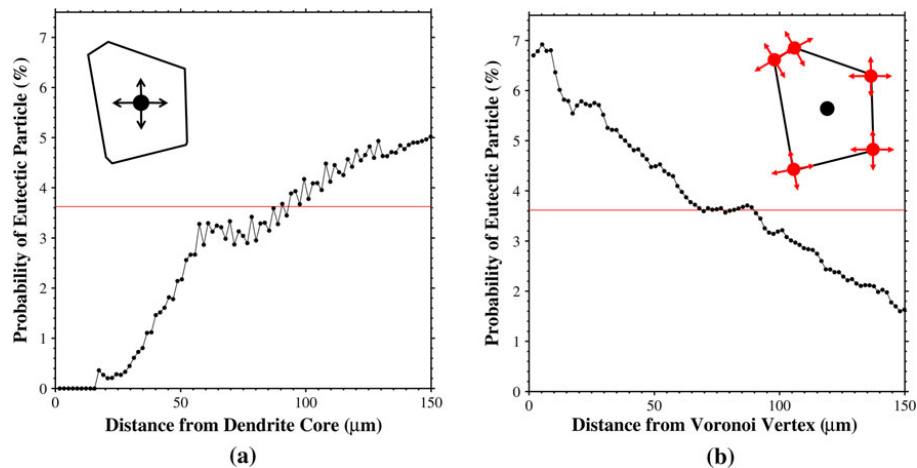
Fig. 11—The probability of a eutectic particle as a function of the distance to (*a*) the nearest dendrite core or (*b*) the nearest Voronoi vertex. The inset schematic shows the reference point(s) for the Euclidean distance in each plot.
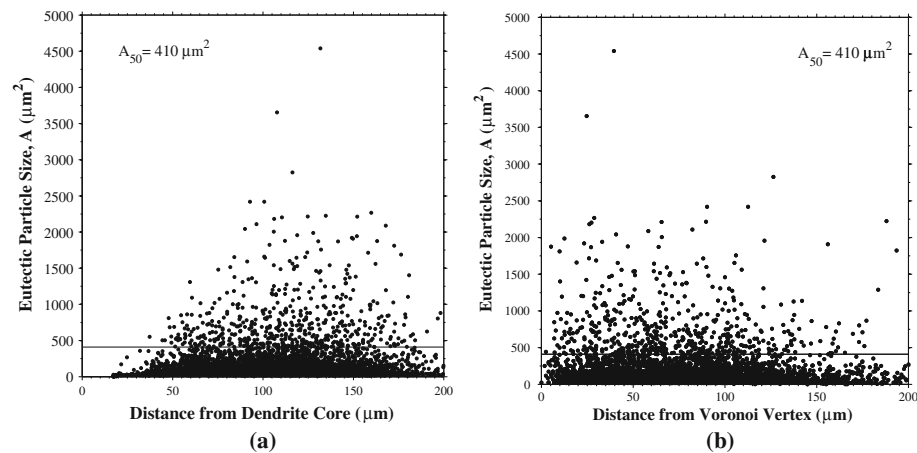

Fig. 12—The eutectic particle size as a function of the distance to (*a*) the nearest dendrite core or (*b*) the nearest Voronoi vertex. The distance for each particle is the distance for the particle centroid. The 50th-percentile area, $A_{50} = 410\ \mu m^2$, refers to the particle size where 50 pct of the eutectic particle area lies above/below this size.

is not favorable for eutectic particles to form close to the primary dendrite core.

Figure 11(b) is a similar plot as a function of distance from the vertices of the Voronoi tessellation (see schematic). This plot was generated in a similar manner to Figure 11(a); a Euclidean distance map was first formed from the Voronoi vertices, then the boundary pixels within 100 μm of the image boundaries were excluded, *etc*. There is an increased occurrence of eutectic particles at vertices, regardless of their distance from the dendrite core. This observation (along with the fact that the probability of occurrence is higher than in Figure 11(a) by almost 2 pct) suggests that solute is

forced near the Voronoi vertices, thereby increasing the probability of eutectic particle occurrence. The transition distance in this plot is between 67 and 90 μm, *i.e.*, at ~1/3 of the PDAS. While this analysis shows the preferential formation of eutectic particles based on the local distances, correlation with the size of particles is also important.

The eutectic particle size may be correlated with the distance from the dendrite cores or Voronoi vertices as well. Figure 12 shows the eutectic particle size as a function of the distance from the nearest dendrite core and the nearest Voronoi vertice. The solid line shows the 50th-percentile area, $A_{50} = 410\ \mu m^2$, which refers to the
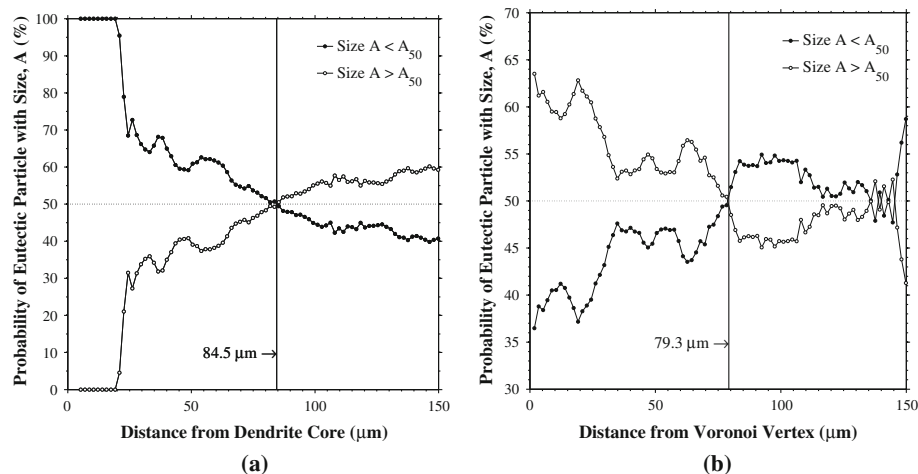
Fig. 13—The probability of a eutectic particle of a certain size occurring as a function of the distance to (*a*) the nearest dendrite core or (*b*) the nearest Voronoi vertex. Two particle sizes are considered: particle sizes below and above the 50th-percentile area A_{50}. The solid line denotes the distance at which the probability functions first intercept, indicating a transition from the favorability of small particles to large particles (a) or *vice versa* (b).

eutectic particle size where 50 pct of the eutectic particle area lies above/below this size. There is a noticeable tendency for the larger particles ($A > A_{50}$) to form further away from the dendrite core and closer to the Voronoi vertices, while the smaller eutectic particles ($A < A_{50}$) can form at all distances. However, it is difficult to quantitatively tell from the following plot what the preference is for smaller or larger particles as a function of distance. Therefore, to further quantify this relationship with respect to the size of the particles, the probability associated with a eutectic particle pixel belonging to either a small or large particle is calculated in Figure 13. Interestingly, in Figure 13(a), at distances closer to the dendrite cores, there is a clear preference for smaller particles ($A < A_{50}$) to form over larger particles ($A > A_{50}$). At a distance of 84.5 μm (~1/3 PDAS), as denoted by the solid line, there is a crossover in the probability function and larger particles are statistically favored to form over smaller particles. In the case of distances from the Voronoi vertices, there is a similar behavior except that *larger* particles are favored at smaller distances (closer to Voronoi vertices). The crossover in the probability functions occurs at 79.3 μm (~1/3 PDAS again). At distances greater than this, there is not as definitive of a trend as with the dendrite cores, *i.e.*, in some cases, there is a greater probability for smaller particles to form and, in some cases, for larger particles to form. Clearly, the distance from the dendrite cores and, hence, the local PDAS affect the probabilities of interdendritic particles to form, though. In a similar manner, it is anticipated that a similar relationship may be associated with shrinkage porosity, gas porosity, and other interdendritic defects.

IV. CONCLUSIONS

Characterizing the PDAS in directionally solidified microstructures is an important step for developing process–structure–property relationships by enabling the quantification of (i) the influence of processing on microstructure and (ii) the influence of microstructure on properties. Thin-walled directionally solidified structures (*e.g.*, a turbine blade) require new approaches for characterizing the dendrite arm spacing and the microstructure. In this work, we utilized a new Voronoi-based approach for spatial point pattern analysis that was applied to an experimental dendritic microstructure. This technique utilizes a Voronoi tessellation of space surrounding the dendrite cores to determine nearest neighbors and the local PDAS. In addition, we compared this technique to a recent distance-based technique, the Warnken–Reed method, and a modification to this using Voronoi tessellations, along with the minimal spanning tree method. Moreover, a convex hull-based technique was used to include edge effects for such techniques, which can be important for thin specimens. These methods were used to quantify the distribution of local PDASs as well as their spatial distribution for an experimental directionally solidified superalloy micrograph. Last, eutectic particles were segmented to correlate distances from dendrite cores and Voronoi vertices to the occurrence and size of these interdendritic features. Interestingly, with respect to the distance from the dendrite core, it was found that there is a greater probability of occurrence of large eutectic particles (>410 μm) over small particles at distances greater than ~1/3 of the bulk-measured PDAS. This systematic study of the different techniques for

34

quantifying local PDASs, and their effect on microstructure, can be an important step for correlating with both processing and properties in single-crystal nickel-based superalloys.

REFERENCES

1. R.C. Reed: *The Superalloys: Fundamentals and Applications.* Cambridge University Press, Cambridge, 2006.
2. T.M. Pollock and S. Tin: *J. Propuls. Power*, 2006, vol. 22 (2), pp. 361–74.
3. H.S. Whitesell and R.A. Overfelt: *Mater. Sci. Eng. A*, 2001, vol. 318 (1–2), pp. 264–76.
4. A.J. Elliott, S. Tin, W.T. King, S.C. Huang, M.F.X. Gigliotti, and T.M. Pollock: *Metall. Mater. Trans. A*, 2004, vol. 35A, pp. 3221–31.
5. M. Melo, E.M.S. Rizzo, and R.G. Santos: *J. Mater. Sci.*, 2005, vol. 40 (7), pp. 1599–1609.
6. M. Lamm and R.F. Singer: *Metall. Mater. Trans. A*, 2007, vol. 38A, pp. 1177–83.
7. C.L. Brundidge, D. Vandrasek, B. Wang, and T.M. Pollock: *Metall. Mater. Trans. A*, 2012, vol. 43A, pp. 965–76.
8. P.N. Quested and M. McLean: *Mater. Sci. Eng. A*, 1984, vol. 65, pp. 171–80.
9. V.A. Wills and D.G. McCartney: *Mater. Sci. Eng. A*, 1991, vol. 145, pp. 223–32.
10. D.G. McCartney and J.D. Hunt: *Acta Metall.*, 1981, vol. 29 (11), pp. 1851–63.
11. J. Hui, R. Tiwari, X. Wu, S.N. Tewari, and R. Trivedi: *Metall. Mater. Trans. A*, 2002, vol. 33A, pp. 3499–3510.
12. W. Wang, P.D. Lee, and M. McLean: *Acta Mater.*, 2003, vol. 51 (10), pp. 2971–87.
13. J.D. Miller and T.M. Pollock: in *Superalloys 2012*, John Wiley & Sons, Inc., Hoboken, 2012, pp. 653–62.
14. C.L. Brundidge, J.D. Miller, and T.M. Pollock: *Metall. Mater. Trans. A*, 2011, vol. 42A, pp. 2723–32.
15. B.C. Wilson, E.R. Cutler, and G.E. Fuchs: *Mater. Sci. Eng. A*, 2008, vol. 479 (1–2), pp. 356–64.
16. M.C. Flemings: *Metall. Trans. A*, 1974, vol. 5A, pp. 2121–34.
17. H. Jacobi and K. Schwerdtfeger: *Metall. Trans. A*, 1976, vol. 7A, pp. 811–20.
18. S.N. Tewari, Y.H.S. Weng, G.L. Ding, and R. Trivedi: *Metall. Mater. Trans. A*, 2002, vol. 33A, pp. 1229–43.
19. U. Paul, P.R. Sahm, and D. Goldschmidt: *Mater. Sci. Eng. A*, 1993, vol. 173, pp. 49–54.
20. M.A. Tschopp, A.L Oppedal, J.D. Miller, M.A. Groeber, A.H. Rosenberger, and K.N. Solanki: in *Characterization of Minerals, Metals and Materials 2013*, John Wiley & Sons, Inc., Hoboken, 2013, pp. 299–310.
21. N. Warnken and R.C. Reed: *Metall. Mater. Trans. A*, 2011, vol. 42A, pp. 1675–83.
22. N. Warnken and R.C. Reed: *IOP Conf. Ser. Mater. Sci. Eng.*, 2011, vol. 27, pp. 1–5.
23. C. Dussert, G. Rasigni, M. Rasigni, J. Palmari, and A. Llebaria: *Phys. Rev. B*, 1986, vol. 34 (5), pp. 3528–31.
24. B. Billia, H. Jamgotchian, and H.N. Thi: *Metall. Trans. A*, 1991, vol. 22A, pp. 3041–50.
25. P. Peng, X.Z. Li, Y.Q. Su, D.M. Liu, J.J. Guo, and H.Z. Fu: *J. Mater. Res.*, 2013, vol. 28 (5), pp. 740–46.
26. J.D. Miller: Ph.D. Thesis, University of Michigan, 2011.
27. M.A. Tschopp, M.A. Groeber, R. Fahringer, J.P. Simmons, A.H. Rosenberger, and C. Woodward: *Scripta Mater.*, 2010, vol. 62 (6), pp. 357–60.
28. M.A. Tschopp, M.A. Groeber, J.P. Simmons, A.H. Rosenberger, and C. Woodward: *Mater. Charact.*, 2010, vol. 61 (12), pp. 1406–17.
29. M.A. Tschopp, M.A. Groeber, R. Fahringer, J.P. Simmons, A.H. Rosenberger, and C. Woodward: *Model. Simul. Mater. Sci. Eng.*, 2010, vol. 18, p. 025014.

4 Metallurgical and Materials Transactions A Paper, October 2015

M.A. Tschopp, J.D. Miller, A.L. Oppedal, K.N. Solanki, Evaluating Local Primary Dendrite Arm Spacing Characterization Techniques Using Synthetic Directionally Solidified Dendritic Microstructures, Metallurgical and Materials Transactions A. 46 (2015) 4610–4628.

Evaluating Local Primary Dendrite Arm Spacing Characterization Techniques Using Synthetic Directionally Solidified Dendritic Microstructures

MARK A. TSCHOPP, JONATHAN D. MILLER, ANDREW L. OPPEDAL, and KIRAN N. SOLANKI

Microstructure characterization continues to play an important bridge to understanding why particular processing routes or parameters affect the properties of materials. This statement certainly holds true in the case of directionally solidified dendritic microstructures, where characterizing the primary dendrite arm spacing is vital to developing the process–structure–property relationships that can lead to the design and optimization of processing routes for defined properties. In this work, four series of simulations were used to examine the capability of a few Voronoi-based techniques to capture local microstructure statistics (primary dendrite arm spacing and coordination number) in controlled (synthetically generated) microstructures. These simulations used both cubic and hexagonal microstructures with varying degrees of disorder (noise) to study the effects of length scale, base microstructure, microstructure variability, and technique parameters on the local PDAS distribution, local coordination number distribution, bulk PDAS, and bulk coordination number. The Voronoi tesselation technique with a polygon-side-length criterion correctly characterized the known synthetic microstructures. By systematically studying the different techniques for quantifying local primary dendrite arm spacings, we have evaluated their capability to capture this important microstructure feature in different dendritic microstructures, which can be an important step for experimentally correlating with both processing and properties in single crystal nickel-based superalloys.

I. INTRODUCTION

MICROSTRUCTURE imaging and characterization are an important bridge to understanding why particular processing routes or parameters affect the properties of materials. Developing an enhanced understanding of mechanical behavior in materials relies upon sufficiently characterizing microstructure details at the relevant length scales that contribute to this behavior. Moreover, to truly enhance the predictive capability of processing–structure–property models that aim to improve material performance requires a quantitative stereological description of the relevant microstructure features and, thereby, the material itself. Predictive models that effectively capture the linkage between processing and properties (through microstructure) can be utilized within an integrated computational materials engineering approach to design materials and accelerate their insertion into application.

As crystallographic texture and grain boundary properties are instrumental to the properties and performance of some materials, processing routes that produce directionally solidified dendritic microstructures have emerged as a way to remove adverse effects of grain boundaries that are observed in some materials applications. One such application is in turbine blades within the high temperature section of the modern turbine engine, where single crystal nickel-based superalloys are widely used.[1,2] In single crystal nickel-based superalloys, there are a number of length scales of microstructure that contribute to mechanical behavior, ranging from the γ' precipitates to pores and eutectic particles to the dendrites themselves. At the largest microstructure length scale in directionally solidified single crystal microstructures, the features of interest are the dendrites; many features at lower length scales (e.g., eutectic particles, precipitates) or at similar scales (e.g., porosity, freckle defects) are strongly associated with the dendrite arm spacing and morphology.[3–7] The solidification morphology associated with dendrite arm spacing has been described in the literature.[8,9]

Historically, the primary dendrite arm spacing (PDAS) has been found to correlate with processing (e.g., solidification/cooling rate)[7,10–17] as well as with properties (e.g., creep strength, fatigue properties).[6,16,18] Lamm and Singer[6] produced single crystal

MARK A. TSCHOPP, Materials Engineer, is with the US Army Research Laboratory, Aberdeen Proving Ground, MD 21005. Contact e-mail: mark.a.tschopp.civ@mail.mil JONATHAN D. MILLER, Senior Materials Research Engineer, is with the Air Force Research Laboratory, Wright-Patterson AFB, OH 45433. ANDREW L. OPPEDAL, Research Professor, is with the Center for Advanced Vehicular Systems, Mississippi State University, Mississippi State, MS 39762. KIRAN N. SOLANKI, Assistant Professor, is with the School for Engineering of Matter, Transport, and Energy, Arizona State University, Tempe, AZ 85287.
Manuscript submitted December 19, 2014.
Article published online May 20, 2015

nickel-based microstructures (PWA 1483) with a varied range of different dendrite arm spacings (250 to 600 μm). In their study, they found that decreasing the mean dendrite arm spacing was associated with an increased high-cycle fatigue life, because the fatigue cracks tended to originate at shrinkage porosity; the largest shrinkage pores correlated with a large PDAS. Similar observations of a correlation between dendrite arm spacings and microporosity or solute segregation has been observed by researchers as well.[7,15,17] On the processing side, manufacturing turbine blades via the liquid metal cooling (LMC) process[4,14,19,20] enables a greater degree of control over the size of the primary dendrite arm spacing because of the higher thermal gradient associated with this process. For example, Franke et al.[21] summarizes several recent studies comparing the LMC process and the conventional high rate solidification process. In each case considered, the LMC process resulted in a smaller primary dendrite arm spacing and an improved withdrawal speed. Additionally, some researchers are exploring the use of magnetic fields to complement directional solidification processes and further reduce the primary dendritic arm spacing.[22–24] The use of various processing techniques such as LMC may allow thermal gradients, and hence primary dendrite arm spacing, to be tailored towards a (more desirable) lower mean primary dendrite arm spacing and more homogeneous primary dendrite arm spacing.[14]

The identification of the primary dendrites in these studies is required to quantify the effect of processing/alloying on the microstructure. In many experimental studies of dendrite arm spacing, the dendrite core is typically identified manually in the experimental micrographs. In light of some of the larger dendrite datasets and images, there are some automated image processing methods that have been investigated to identify dendrite core locations by exploiting their fourfold symmetry.[25] Some researchers[26] have highlighted some of the difficulties in identifying dendrite arm spacing from microstructure and have suggested modified alternatives based on dendrite trunk diameters,[27] which may also be useful for correlating with solidification processing parameters. Hence, for understanding the role of dendrite arm spacing in future alloys and processing routes, a confluence of automated experimental techniques for attaining microstructures, automated techniques for identifying dendrites, and automated (and informed) characterization techniques is required.

The traditional approach for measuring primary dendrite arm spacing in single crystal metals, whereby the number of dendrite cores in a specified area is related to the dendrite arm spacing[10,28,29] is given by:

$$\lambda = c\sqrt{\frac{A}{n}} \qquad [1]$$

where λ is primary dendrite arm spacing, A is the area analyzed, n is the number of dendrites, and c is a coefficient that depends on the microstructure. McCartney and Hunt[10] showed that $c = 0.5$ for a random array of points, $c = 1$ for a square array of points, and $c = 1.075$ for a hexagonal array of points; they had to apply a correction for the bulk dendrite arm spacing λ as processing conditions caused a change in the local environment of the dendrites, i.e., a transition from cellular growth to dendrite growth.[10,11,30] However, this approach is insufficient for capturing local arm spacings or the dendrite arm spacing distribution, and may provide problems with complex geometries such as turbine blades. In fact, part of the motivation for quantifying the local PDAS is that a narrow distribution (i.e., low standard deviation) of local PDAS values may result in a more homogeneous distribution of interdendritic microstructure features and, more importantly, a narrow distribution of mechanical properties.[31] Structural inhomogeneities in single crystal components, which may cause wider property variations, have been correlated to asymmetric heat flux and transients in solidifications.[32]

Previous work examined some recent approaches, as well as some modified versions of these approaches, for characterizing the local dendrite arm spacing within experimental dendritic microstructures.[33] This work used an experimental dendritic microstructure along with three different techniques that are based on the nearest neighbor spacing and/or a Voronoi tesselation of the dendrite cores. Figure 1 shows (a) an example of a directionally solidified dendritic microstructure[34] along with contour plots showing the evolution of the local PDAS as a function of dendrite location for four different techniques (to be discussed in Section II–B). This study found that augmenting existing techniques with Voronoi tesselations resulted in a more physical description of the local dendrite arm spacing and resulted in a mean PDAS that compared favorably to the traditional bulk characterization technique (Eq. [1]). However, several questions remained. For example, while comparing the mean of the local PDAS with the bulk PDAS calculated from Eq. [1] is a valid method for examining the validity of the local characterization techniques, an experimental microstructure contains some degree of disorder. Hence, it is not clear whether these techniques are accurately capturing both the local PDAS and the local coordination number, since an experimental microstructure may contain regions of fourfold coordination and sixfold coordination. Since the coordination number may bias the local PDAS calculation, it is important to understand the extent to which these techniques capture both local measures.

Therefore, the research objective of the present work is to understand the ability of these Voronoi-based techniques to capture local microstructure statistics (primary dendrite arm spacing and coordination number) in controlled (synthetically generated) microstructures. To meet this objective, cubic and hexagonal synthetic microstructures with varying degrees of disorder (noise) were generated to study the effects of length scale, base microstructure, microstructure variability, and technique parameters on the local PDAS distribution, local coordination number distribution, bulk PDAS, and bulk coordination number (calculated as the mean of the local statistics).

The paper is organized as follows. Section II defines the methodology used herein, including the methods
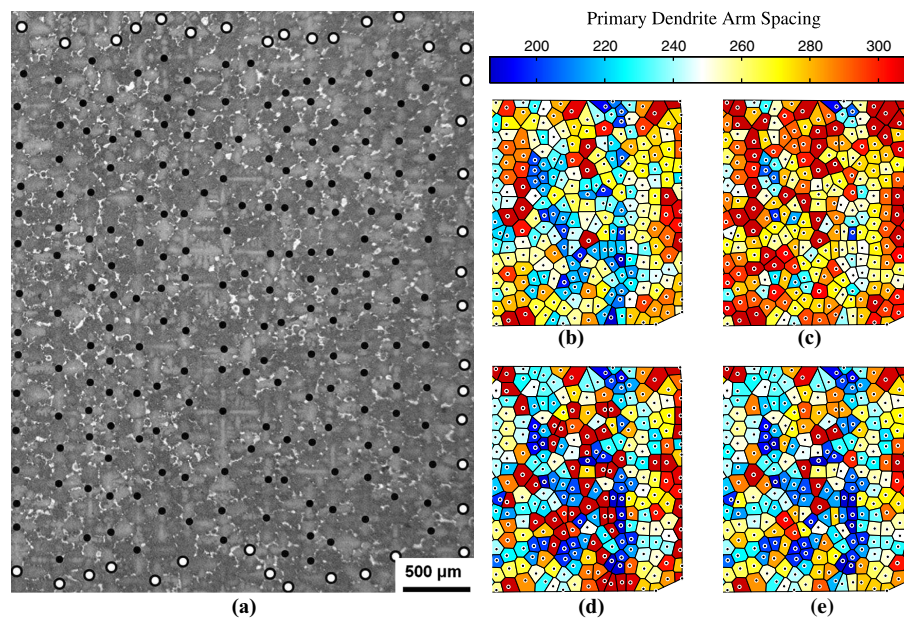
Fig. 1—(a) Example of dendritic structure normal to the withdrawal direction in a directionally solidified single crystal nickel-based superalloy cast using the liquid metal cooling technique.[34] The dots denote the dendrite cores, where the white dots indicate dendrite cores at the edge of the field of view. The local primary dendrite arm spacing (μm) was calculated using four different techniques:[33] (b) Voronoi tesselation with $d_{crit} = 0.12$, (c) Voronoi tesselation with $d_{crit} = 0.00$, (d) Warnken–Reed technique with $\alpha = 2.0$, and (e) Voronoi Warnken–Reed with $\alpha = 2.0$.

used to generate the synthetic microstructures, the different techniques used to quantify the local PDAS, and the simulation test matrix that was performed. Section III presents the results, analysis, and discussion based on the various sets of simulations that were performed. This includes studies on the effect of the microstructure length scale; the effect of microstructure variability and technique parameters on the bulk responses; the effect of microstructure variability and technique parameters on the local distributions; and the correlation between different local measures. Section IV presents the conclusions. The significance of the present work is that it aims to answer several questions pertaining to how to measure the local primary dendritic arm spacing in experimental dendritic microstructures.

II. METHODOLOGY

A. Synthetic Microstructure Generation

Synthetic microstructures were used to assess the ability of the different methods examined within to capture perturbations from two symmetric arrangements: the 4-nearest neighbor cubic cell and the 6-nearest neighbor hexagonal cell. In addition to the perturbations from the ideal cubic and hexagonal configurations, a microstructure with complete randomness of points was generated using random number generators to create N independent points with coordi-

nates R_x and R_y for their respective x and y coordinates within the appropriate bounds. Figures 2(a) through (c) illustrates the three different types of patterns used in the present study. The random pattern was added to quantify when the perturbations for a specific pattern became indistinguishable from a random set of points.

The degree of deviation from the ideal symmetric configurations was then systematically introduced. Previous methods have used a uniform or Gaussian distribution of noise in both the x and y directions for all points or have utilized a combination of the fraction of points perturbed as well as the distance shifted. Here, we have utilized a uniform distribution of noise that is a fraction of the nearest neighbor distance a_0. Figures 2(d) through (f) shows three different noise levels for a 10 × 10 cubic pattern, whereby the lines illustrate the degree of deviation from the starting base lattice. As noise is increased, the starting lattice becomes less recognizable as it moves towards a purely random configuration of points. However, the ability to characterize the local environment of a point in the presence of these perturbations and relate this to a base microstructure lattice presents a number of challenges. The subsequent subsection will discuss the techniques that are used herein to characterize such microstructures.

Dendrites near the free surface complicate the analysis of the PDAS statistics. These have been addressed previously using a convex hull and Boolean operations to enable computing of localized statistics using Voronoi tesselations. Figure 2(g) shows both interior points
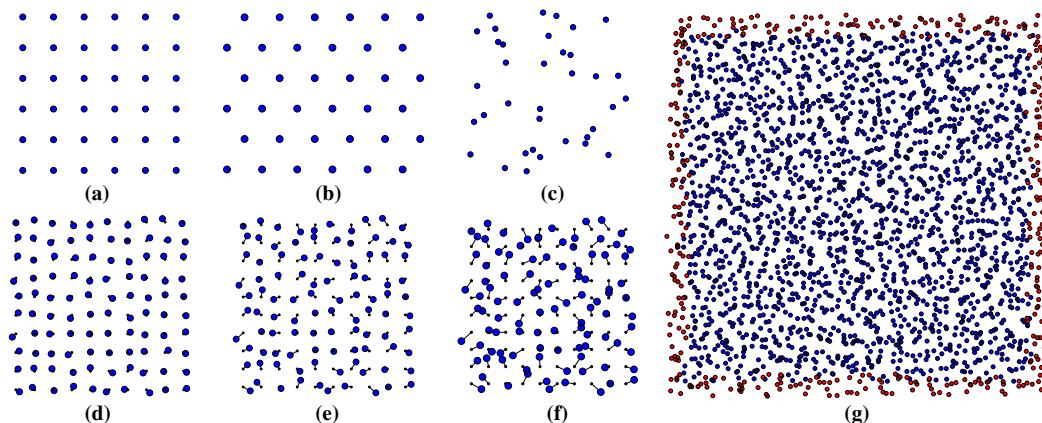
Fig. 2—Three different types of patterns were used in the present study: (*a*) cubic pattern, (*b*) hexagonal pattern, and (*c*) random pattern. Three different microstructures show the effect of the noise level of (*d*) $0.20a_0$, (*e*) $0.40a_0$, and (*f*) $0.60a_0$. As an illustration of the deviation from the perfect cubic array of points, the original coordinates of the cubic pattern (*i.e.*, Fig. 2(a)) is shown as a black dot with a line connecting it to the deviated coordinate (large blue dots). For this particular 10×10 pattern, as the noise level is increased, the same points are shifted in the same direction; the only change is in the magnitude of the shift. (*g*) To eliminate edge effects, statistics from points on the exterior of the area are excluded. However, these points are still used to evaluate statistics in points on the interior region.

(blue) and edge points (red) for the large microstructures, whereby the edge points are selected using a small distance ($1.5a_0$) from edge of the microstructure pattern. The present analysis includes these edge points only for calculating the localized statistics of interior points, but does not use their localized statistics for subsequent mean statistics, heretofore also referred to as the bulk statistics. In this sense, the present paper focuses on locally measured statistics and their mean responses (*i.e.*, the bulk PDAS and bulk coordination number) within a bulk microstructure.

Last, it should be mentioned that there are no rules during the generation step that prohibit these microstructures from having two neighboring points that are in close proximity to one another (*e.g.*, the random microstructure in Figure 2(c)). In an experimental microstructure, the primary dendrite cores are separated by a critical minimum distance that should scale with both the size of the dendrite stalk and the distance associated with the transition of tertiary to primary dendrite arms. For example, our previous study[33] shows that the dendrite stalk diameter is approximately 20 pct of the bulk PDAS (*i.e.*, stalk diameter is twice the maximum distance at which no eutectic particles were observed). This prior result suggests that noise levels of $0.40a_0$ are the highest noise level that might be observed in a real microstructure, because any higher noise level could produce neighboring points that lie within $0.20a_0$ distance of each other. However, this estimation of the trunk diameter is only an estimation—other studies have shown that the trunk diameter itself may be a useful criterion for understanding directional solidification and its impact on microstructure.[27] While not examined herein, microstructures built using a shell model or random sequential adsorption algorithms (*e.g.*, Reference 35) could allow researchers to understand how this critical

minimum distance affects the local PDAS results. In general, though, the higher degrees of noise in the synthetic microstructures allow us (1) to capture and understand the trends in mean PDAS behavior, and (2) test the capability of these different algorithms to handle some potentially extreme scenarios (of 2 or more points lying close to one another). Furthermore, the results show that the random microstructures primarily comprised a mixture of 4-, 5-, and 6-coordinated points, in agreement with experimental microstructures.

B. *Local Characterization Techniques*

The approach utilized herein to measure the local dendrite arm spacing is based on a Voronoi tesselation of the spatial array of dendrite cores. The following analysis techniques were implemented in MATLAB R2014 (The MathWorks, Inc.). To illustrate how the present method works and differs from some other published methods, a synthetic 5×5 cubic pattern of points is generated with varying degrees of noise (100 pct noise fraction and noise fraction as in References 36, 37), as shown in Figure 3. In Figure 3, the different techniques for the same microstructure are shown from left to right (labels at the bottom), while the noise level is increased from top to bottom to illustrate the differences. The techniques presented in Figure 3 were first used together in Tschopp *et al.*[33] to characterize the local spacing for an experimental microstructure of a directionally solidified single crystal nickel-based superalloy. In contrast to that work, the following work will examine the sensitivity and applicability of a few of these techniques based on thousands of synthetic microstructure instantiations.

Figure 3 shows several methods for characterizing the local microstructure environment. One such method for
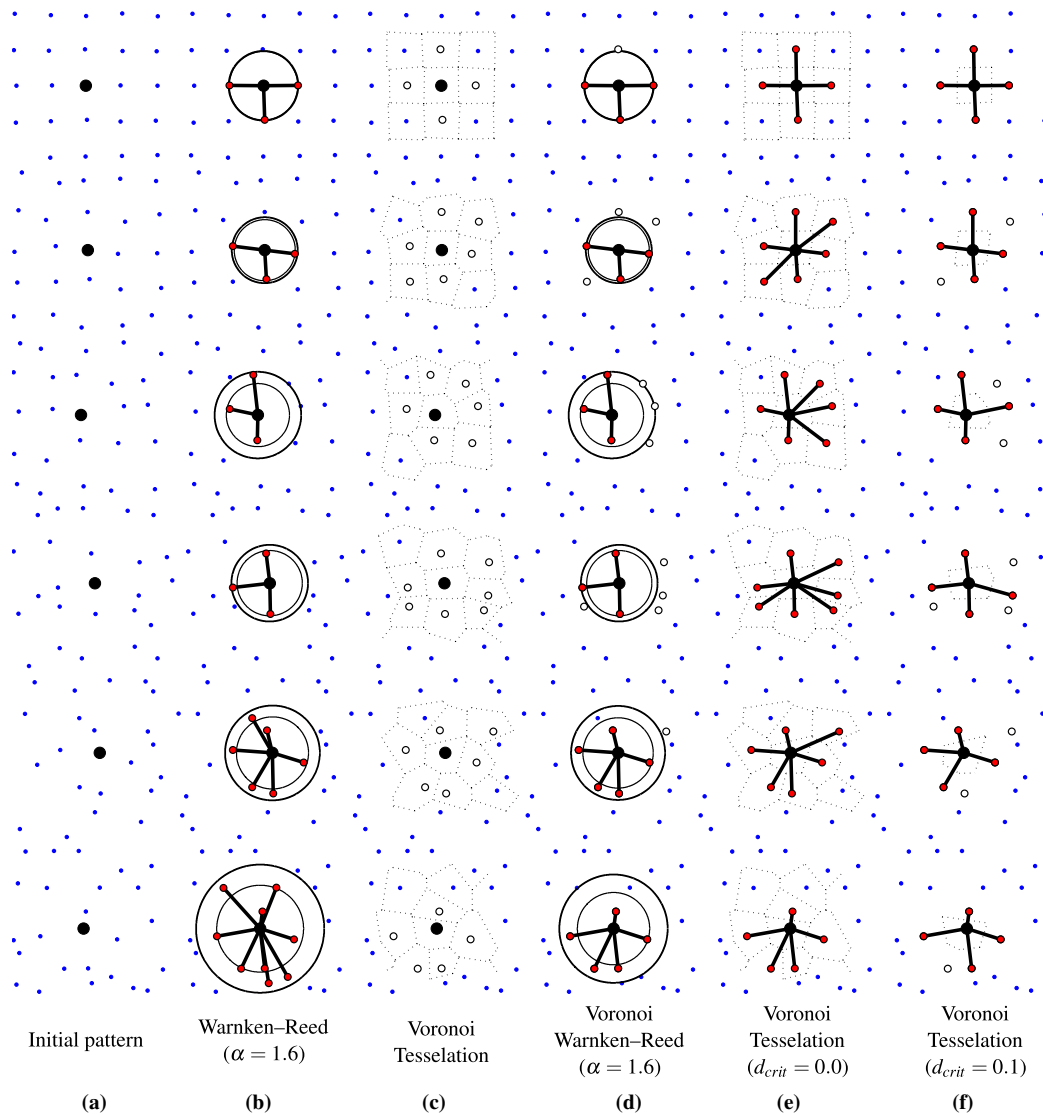
Fig. 3—The difference between various methods for defining the nearest neighbors (red dots) and their spacing for a single point (large black dot) with a distorted local environment. Images in (*a*) through (*f*) are (a) the initial pattern, (b) the Warnken–Reed method with $\alpha = 1.5$ and $k_{initial} = 3$, (c) the Voronoi tesselation diagram for the points, (d) the Voronoi-modified Warnken–Reed method with $\alpha = 1.5$ and $k_{initial} = 3$, (e) the Voronoi method ($d_{crit} = 0.0$), and (f) the modified tesselation-based technique with $d_{crit} = 0.10$.

measuring the local dendrite arm spacing is the Warnken–Reed method.[36,37] The Warnken–Reed method calculates the dendrite arm spacing for a single point (black dot) by starting with an initial number of nearest neighbors, $k_{initial}$ (often $k_{initial} = 3$, *i.e.*, three closest neighbors), and then iteratively adding potential nearest neighbors that are within a cutoff distance defined by the already-added nearest neighbors. The inner circle in the second and fourth column of Figure 3

represents the average spacing, d_{avg}, of these neighbors and the outer circle represents the cutoff for adding the next neighbor, $d_{avg} + \alpha d_{std}$, where d_{std} is the standard deviation of the nearest neighbor spacings and α is a parameter that is typically between 1 and 2. Neighbors continue to be added until the cutoff does not include any new neighbors. The local coordination number and dendrite arm spacing is calculated from the neighbors added (shown as red dots in Figure 3). However, if the

standard deviation of the distances of the nearest neighbors d_{std} or the parameter α is large, this technique can continue to add nearest neighbors beyond the first nearest neighbors. Notice that the distance between the inner and outer circle tends to increase with increasing noise due to the increased d_{std} of the nearest neighbors. As discussed in Tschopp et al.,[33] clearly a method for restricting the number of nearest neighbors using such a technique is necessary.

Another method of identifying the potential of first nearest neighbors is to perform a Voronoi tesselation of the space surrounding the points, as shown in the third column of Figure 3. The polygon edges are equidistant between the points contained in the two adjacent polygons and the triple points (merging of three lines) are equidistant between the points contained in the three adjacent polygons. Therefore, the first nearest neighbors (FNNs, shown as open circles in Figure 3) correspond to the edges of the central polygon (that contains the black dot). This subset of points is the maximum number of nearest neighbors that the central point can have.

In this manner, several techniques have been identified to quantify a local dendrite arm spacing based on the Voronoi-identified FNNs.[33] For example, the Voronoi Warnken–Reed (VWR) method (Figure 3) only includes the Voronoi FNNs as potential nearest neighbors and cannot expand beyond these, alleviating a potential problem of selecting second-nearest neighbors or greater. Another method using the Voronoi FNNs is to consider all of these potential nearest neighbors as nearest neighbors (Figure 3), as in Brundidge et al.[15] Unfortunately, this approach is sensitive to small perturbations in the spatial positions of the neighbors. Notice that a small degree of noise added to the cubic lattice (in row 2) results in several more nearest neighbors being identified. As the corresponding edge of the polygon for these 45 deg points is small, a slight movement away from the central point would cause this point to no longer share an edge with the polygon containing the black dot; in this scenario, the two adjacent polygons on either side would effectively "pinch" off this neighbor. This scenario, however, has a physical basis in solidification microstructures as these can be envisioned as two dendrite cores that compete with the central core, and the 45 deg cores have a much less prominent effect on the central core.

The last method utilizes a criterion based on the edge lengths of the Voronoi polygon.[33] In Figure 3, those neighbors with edge lengths less than a critical fraction, d_{crit}, of the total polygon perimeter are excluded as nearest neighbors (e.g., 10 pct in Figure 3). In the present study, the local dendrite arm spacing statistics are evaluated using two of these four techniques: VWR and the Voronoi technique with ($d_{crit} \geq 0$) a line length threshold.

With respect to the addition of noise to the 5×5 cubic pattern, these methods handle the increased levels of noise very differently. First, the distance-based Warnken–Reed method does not incorporate enough neighbors at low noise levels and incorporates many more neighbors at higher noise levels than the Voronoi-based techniques (rightmost two columns). The use of the Voronoi-identified nearest neighbors to limit the

number of neighbors selected does seem to improve the technique in a physical manner for higher noise levels. For several noise levels, the Voronoi method with $d_{crit} = 0.0$ does clearly overestimate the number of nearest neighbors, while the four nearest neighbors identified through $d_{crit} = 0.1$ (Figure 3) perhaps offers a better approximation of the number of nearest neighbors. Interestingly, the Voronoi method with $d_{crit} = 0.1$ does identify four nearest neighbors for all noise levels. Previous work has also shown that while these methods can identify the same number of neighbors, they can in fact be different neighbors.[33] This can be due to the Warnken–Reed method being a distance-based method, and identifying the four closest neighbors, while the modified Voronoi technique is based on the edge lengths of the Voronoi polygon, and hence utilizes this to identify nearest neighbors (which may not be the closest neighbors).

The motivation for examining the sensitivity and capability of these local PDAS metrics is that the traditional PDAS metric does not consider the order or disorder of the dendrites within the microstructure. Figure 3 illustrates why a local metric for PDAS may be needed. For the field of view given in Figures 2 and 3, the bulk PDAS metric would be the same since the number of dendrites n and the area A are equal (see Eq. [1]). However, the increasing disorder of the dendritic structure in the case of Figure 3 may yield (i) a more uneven distribution of solute elements, (ii) the formation of second phase particles, (iii) the formation of gas or shrinkage porosity, or (iv) the lateral growth of secondary dendrite arms. Hence, in addition to the bulk PDAS values, understanding how processing conditions may impact the disorder of the dendritic structure may be important for understanding the properties of directionally solidified alloys.

C. Simulation Test Matrix

The ability to rapidly generate synthetic microstructures of known lattice spacing, noise fraction, and coordination (from the type of pattern utilized) allows for a controlled understanding of how well these computational techniques can estimate the local coordination numbers and local PDAS. First, several studies were explored to understand how these different factors affect the bulk dendrite responses (PDAS and coordination number) based on the mean value of the locally calculated statistics; in this manner, these mean responses can be directly compared with the known bulk PDAS and the coordination number (for a zero-noise microstructure). Next, a series of simulations were performed to examine the local response and how this changes as a function of these different factors. In doing so, the present work aims to answer several questions pertaining to how to measure the local primary dendritic arm spacing in experimental microstructures, as posed in the following 4 studies.

1. What is the effect of the microstructure length scale on bulk (or mean) PDAS measurements? In particular, the goal of this analysis is to understand

how changing the number of dendrites (points) captured within an image (field of view) relates to the overall dendrite arm spacing. This set of simulations varied several parameters to understand this variability: the length scale of the field of view (*i.e.*, the number of points/dendrites), the type of pattern used (Figure 2), and the type of method used (VWR, Voronoi). Twenty microstructure instantiations were used at a noise fraction of $0.40a_0$ ($a_0 = 1$).

2. What is the effect of the parameters for the different methods (VWR, Voronoi) on the bulk PDAS measurements? How does the variability in the microstructure affect these measurement techniques? The goal of this analysis is to understand how α and d_{crit} for the VWR and Voronoi methods affects the measured PDAS and coordination number for different microstructures. Hence, α was varied from 1.0 to 2.0 in increments of 0.1; similarly, d_{crit} was varied from 0.0 to 0.12 in increments of 0.02. The microstructure may also influence the sensitivity of these parameters, so both cubic and hexagonal microstructures were generated with 6 different noise levels: $0.05a_0$, $0.10a_0$, $0.20a_0$, $0.30a_0$, $0.40a_0$, and $0.50a_0$.

3. What is the effect of the parameters (α and d_{crit}) for the different methods (VWR and Voronoi Tesselation techniques, respectively) on the local PDAS and the local coordination number distributions? How is this affected by the base configuration and noise of the microstructure? The goal here is to delve further than the mean statistics and start to understand how these different techniques and their parameters affect the distributions of the local statistics. Hence, the same simulations as described in study #2 will be used, but further analysis will be performed pertaining to the local distributions and how they evolve.

4. What is the correlation between local PDAS calculated at two different parameters for the same technique and same microstructures? What is the correlation between the local PDAS and the local coordination number for microstructures with different noise levels? How is the bulk PDAS linked to the coordination number and noise level? The goal of this analysis is to understand the changes in these local statistics with the parameters for these techniques. In other words, how sensitive is any local PDAS to the parameter chosen? Also, does the coordination number directly (or linearly) correlate with the calculated PDAS? This study will investigate these relationships.

In short, the following set of simulations are performed on different synthetically generated microstructures with varying degrees of disorder to better understand the capability of these sorts of local microstructure characterization techniques as it applies to the problem of measuring the local primary dendrite arm spacing in single crystal microstructures. That being said, these techniques are not restricted to this application, but can also be applied to characterizing local statistics in other systems and problems as well.

III. RESULTS AND DISCUSSION

A. *Microstructural Length Scale Effects on PDAS*

The PDAS was quantified for multiple microstructure instantiations to understand the effect of length scales on two measurement techniques. Twenty different microstructures were generated for six different microstructure lengths: 10 (10×10, *i.e.*, 100 points), 20, 30, 40, 50, and 80. In this example, the spacing between nearest neighbor points/dendrites was chosen to be 1, such that the PDAS statistics would have a mean value of 1 for a noise fraction of 0. Recall that to eliminate edge effects, statistics from points on the exterior of the microstructure are excluded (within 1.5 units of the edges). Three patterns (cubic, hexagonal, and random) were used to assess how the type of base pattern affects PDAS convergence. The noise fraction was chosen to be $0.40a_0$, *i.e.*, large enough to add a significant amount of variability, but not so large as to potentially cause points to overlap (*i.e.*, $0.50a_0$ and above). Two different techniques—VWR and Voronoi—were used to assess the convergence of the PDAS statistics with length scale. The VWR method used $\alpha = 2$ and the Voronoi technique used $d_{crit} = 0.12$. While these techniques can be used to calculate the local PDAS and coordination number, in this case these techniques are used to calculate a bulk PDAS value, which is the mean of the local PDAS values.

The evolution of the bulk PDAS and the standard deviation of the bulk PDAS as a function of the length scale is plotted in Figure 4. In Figure 4(a), there are several features to notice. First, a dotted line is drawn at a PDAS of 1 to indicate the expected PDAS value with a noise fraction of 0. Second, each data point is the mean value of the 20 bulk PDAS quantified for each microstructure instantiation. Similarly, the errors bars are equivalent to one standard deviation of those 20 microstructure instantiations. The error bars are offset slightly for each of the different prescribed length scales to avoid the significantly overlap and aid in visualization. Third, the different symbols indicate the different pattern types used and the different colors delineate the different techniques utilized.

There are several trends evident from Figure 4(a). First, as the length scale (and size) of the microstructure increases, the bulk PDAS values converge quickly, such that the bulk PDAS value is very similar in the 20×20 microstructures to that in the 80×80 microstructures, as would be expected. However, the error bars denote that there is significant variation in the individual bulk PDAS values, which decreases as the length scale of the microstructure field of view is increased. In fact, Figure 4(b) plots the standard deviation of the bulk PDAS values as a function of the microstructure length scale on a log–log scale and shows a similar decrease for all synthetic microstructures; a similar decreasing trend was found for the standard deviation of the bulk coordination number as well. In addition to the trends with respect to the length scales, which is somewhat independent of the type of microstructure and measurement technique, there are trends with respect to the
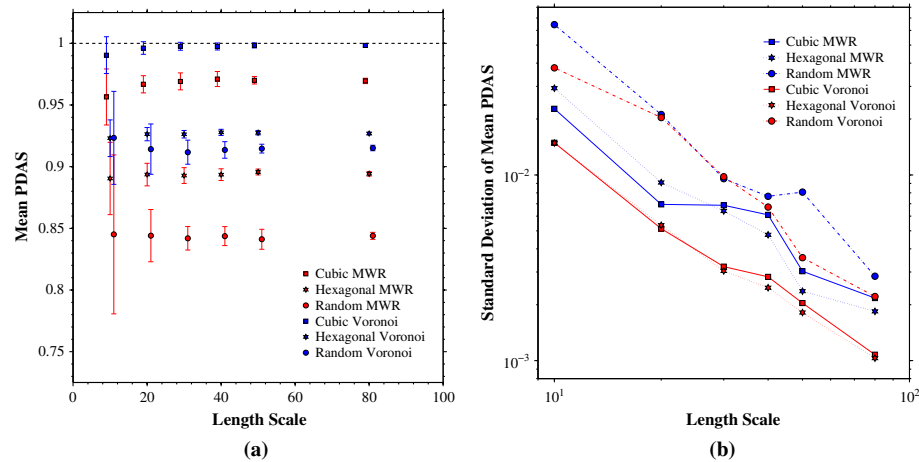
Fig. 4—Evolution of the (*a*) bulk PDAS and (*b*) standard deviation of the bulk PDAS as a function of the length scale. The error bars are for 20 different microstructure instantiations for cubic, hexagonal, and random patterns with a noise fraction of $0.40a_0$. The VWR technique ($\alpha = 2$) and the Voronoi technique ($d_{crit} = 0.12$) were used to calculate the bulk PDAS values for each microstructure.

pattern type and the measurement technique. With both measurement techniques, the cubic pattern is closest to the expected PDAS (without noise), followed by the hexagonal pattern and last the random pattern. For all pattern types, the Voronoi technique was closer to the expected PDAS than the VWR method. Based on these tests, the 80×80 patterns are chosen to illustrate the subsequent trends since multiple microstructure instantiations should not be needed to examine the subsequent trends in terms of microstructure and local PDAS measurement technique.

B. Bulk PDAS and Coordination Number Sensitivity Analysis

The bulk PDAS and bulk coordination number was calculated for multiple microstructures to understand the parameter sensitivity for the two different local PDAS measurement techniques. The α parameter was varied for the VWR method (Figure 5) and the d_{crit} parameter was varied for the Voronoi method (Figure 6). The expected values are represented by the dotted lines in all subfigures (except Figure 5(d) where the bulk bulk coordination numbers significantly underestimate the expected coordination number).

There are several trends that are evident from Figures 5 and 6. In the case of the VWR method, both the bulk PDAS and the bulk coordination number are affected by the parameter α, as has been noted before. As α is increased, the bulk PDAS value increases towards the expected PDAS of 1 and the bulk coordination number increases for all microstructures examined in this study. As the noise level is increased for both the cubic and hexagonal microstructures, the trend is for the bulk PDAS to deviate further from the expected value. However, for high values of α, the bulk PDAS for cubic microstructures with higher noise levels does begin

to approach the expected PDAS at a faster rate than that of the microstructures with lower noise levels (Figure 5(a)). This behavior is a function of two interacting effects: (1) higher α values admitting more nearest neighbors, which have larger spacings (as can be observed in Figure 5(c)), and (2) higher noise levels increase the standard deviation of the nearest neighbor spacings, which (in combination with α) can result in admitting even more nearest neighbors. Interestingly, the bulk coordination number for the hexagonal microstructures in Figure 5(d) does not approach the expected value of 6 for any of the α values chosen. This behavior helps to explain the larger deviation of this technique from the expected PDAS value for hexagonal microstructures in Figure 5(b). However, the inability of this technique to capture the bulk coordination number even for small levels of random noise in hexagonal microstructures ($0.05a_0$) signifies that while it may be useful for exploring some trends between different microstructures, it may significantly under-predict coordination numbers for hexagonal dendritic configurations (which may skew the PDAS statistics as well).

In the case of the Voronoi method, both the bulk PDAS and the bulk coordination number are similarly affected by the parameter d_{crit}. As d_{crit} is increased, the trend is for both the bulk PDAS and bulk coordination number to either decrease or remain constant. The noise level of the cubic or hexagonal microstructure significantly affects the behavior of these responses with respect to d_{crit}. For low noise levels, the Voronoi method with a large d_{crit} value ($d_{crit} \geq 0.04$) captures both the expected PDAS value and the expected coordination number—this behavior indicates that this method is capable of capturing the expected behavior as the noise is reduced to zero, in contrast to the VWR method. The only unusual behavior at low noise levels for the Voronoi method is that obtained for small d_{crit} values
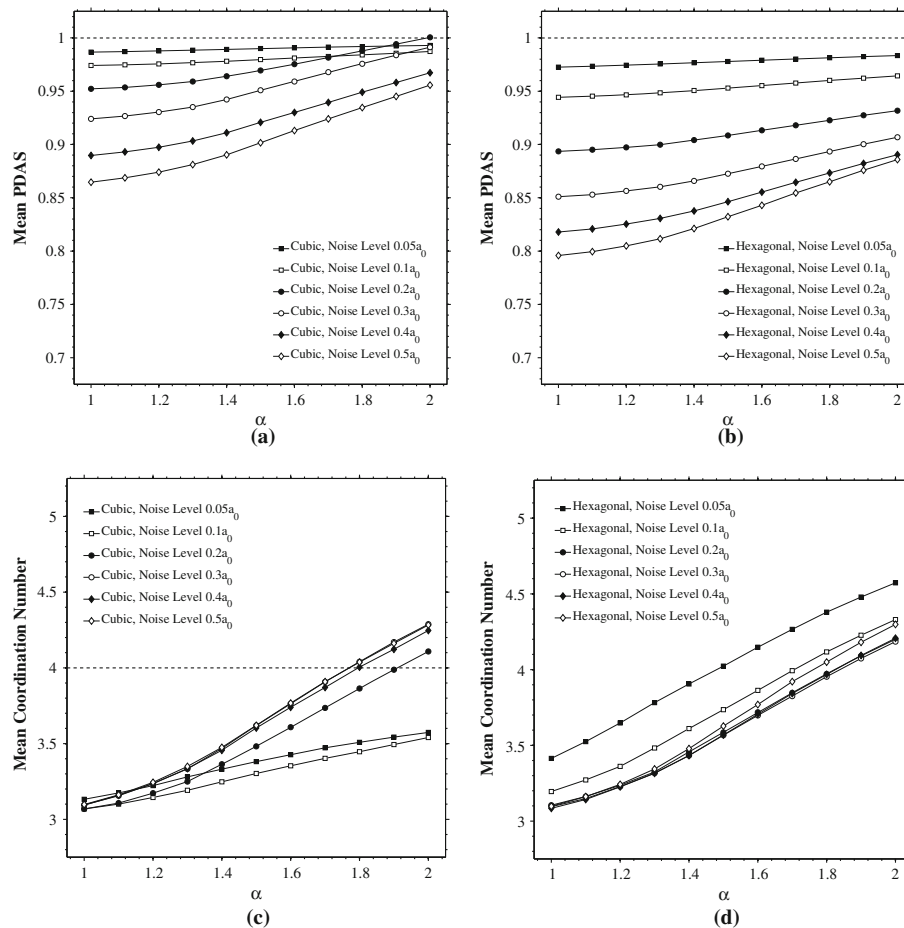
Fig. 5—Evolution of the (*a*, *b*) bulk PDAS and (*c*, *d*) bulk coordination number as a function of the parameter α for the Voronoi Warnkens–Reed method for both (a, c) cubic and (b, d) hexagonal microstructures (80 × 80) with different noise levels. The dotted line represents the expected value for a zero-noise microstructure.

($d_{crit} \leq 0.02$). For $d_{crit} = 0$, the bulk coordination number for the cubic microstructure is 6, regardless of the noise level, because the 4 nearest neighbors always form a face on the Voronoi polygon, while, on average, 2 of the 4 corner neighbors form another face of the polygon (since there is no exclusion of any of the faces (*i.e.*, the d_{crit} parameter), the average coordination number is always 6. In summary, the ability to capture the expected behavior (*i.e.*, zero-noise, ideal microstructures) in microstructures with small noise levels provides some degree of confidence that the Voronoi method with $d_{crit} \geq 0.04$ is a technique that may be appropriate for examining local PDAS and coordination number. Unfortunately, the bulk coordination number (and, consequently, the bulk PDAS) still changes as a function of noise in the microstructure (Figures 6(c) and (d)) and there is no "true" coordination number to evaluate what

exact value of d_{crit} is appropriate. In practice, it should be realized that the choice of the d_{crit} value with the Voronoi technique can affect both the bulk PDAS behavior and the bulk coordination number, but should be appropriate for analyzing trends in microstructures. In the subsequent subsections, the local PDAS and CN calculations over a number of different d_{crit} values for the Voronoi technique will be explored to understand their correlations and the evolution of these distributions.

C. *Local PDAS and Coordination Number Sensitivity Analysis*

The local PDAS and coordination number distributions cause the observed changes in the bulk behavior. To better understand how these distributions change as a function of the d_{crit} value for the Voronoi technique
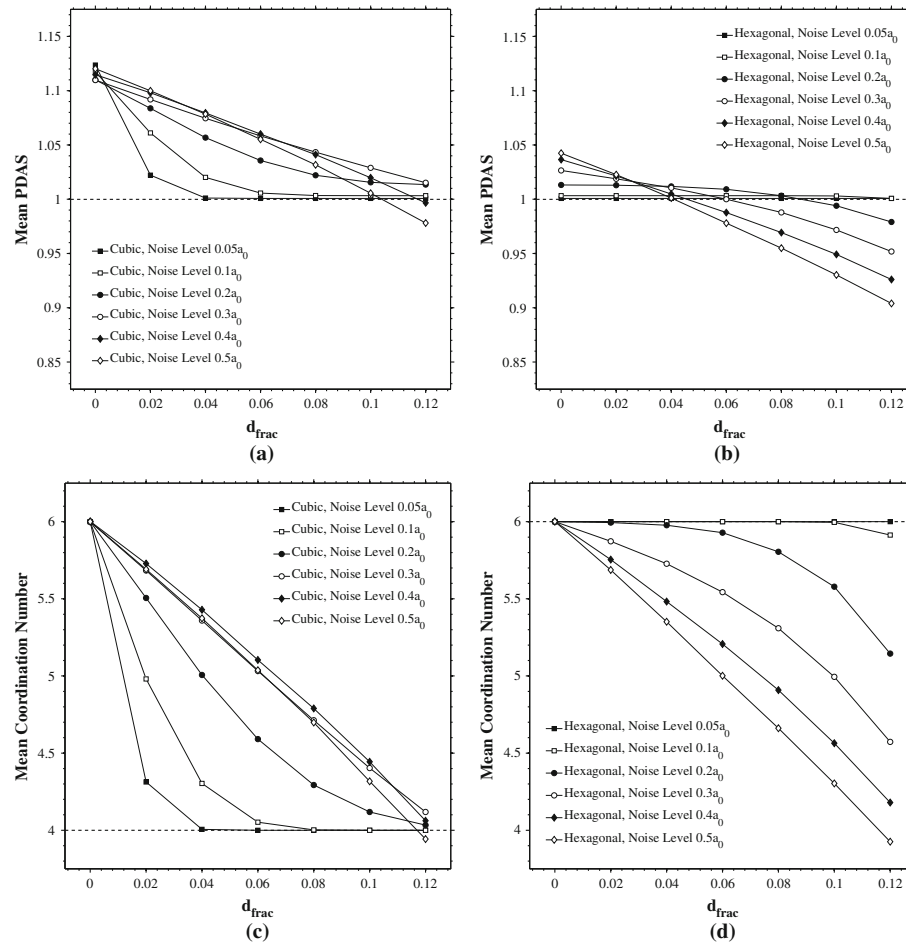
Fig. 6—Evolution of the (*a*, *b*) bulk PDAS and (*c*, *d*) bulk coordination number as a function of the parameter d_{crit} for the Voronoi method for both (a, c) cubic and (b, d) hexagonal microstructures (80 × 80) with different noise levels. The dotted line represents the expected value for a zero-noise microstructure.

(and for α with the VWR technique, not shown), six different noise levels for cubic and hexagonal 80 × 80 microstructures were generated and seven different d_{crit} values were performed for each microstructure. As an example of the probability distribution plots used to show the evolution of local PDAS and coordination with noise, Figure 7 shows their evolution with d_{crit} (multiple lines within each subfigure) for a random microstructure. There are several features within each plot meant to aid in their analysis and comparison. First, each plot displays the local PDAS probability distribution (left plot, red lines) and the local coordination number histogram (right plot, red bars). To delineate the different values of d_{crit}, $d_{crit} = 0$ is shown as a thick maroon line (or thick maroon bar for the coordination number plot) and the remainder of the

lines (bars) indicate monotonic increases in increments of d_{crit} by 0.02. On each plot, the bulk PDAS/coordination numbers for the Voronoi method with various d_{crit} values are shown as blue lines, which are also incremented from 0.00 (right, thick line) to 0.12 (left) in increments of 0.02. Since in some cases these lines may overlap, a circle marker symbol is attached to the line, where the size of the symbol corresponds to the magnitude of d_{crit}. For the case of the random microstructure, increases in d_{crit} decrease the local and bulk PDAS distribution as well as the coordination number distribution. Furthermore, as ordered microstructures (*e.g.*, cubic and hexagonal) approach a more disordered state, the coordination number distribution is more likely to broaden and assume a distribution of different local coordination numbers (with 4, 5, and 6 being the
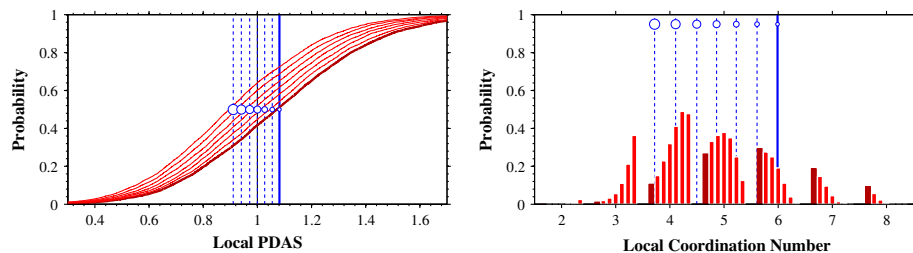
Fig. 7—Cumulative probability plot of the local PDAS (left plot) and coordination number (right plot) distribution as a function of the parameter d_{crit} for the Voronoi method for a random microstructures (80 × 80). The red (dotted blue) line represents the local PDAS/coordination number distribution (bulk PDAS/coordination number) for d_{crit} values of 0.00 (right, thick line) to 0.12 (left) in increments of 0.02.

most frequent). The remainder of this section will focus on the evolution of the local statistics for cubic and hexagonal microstructures with varying degrees of noise.

1. Voronoi technique with cubic microstructures

The local PDAS and coordination number distributions cause the observed changes in the bulk behavior. To better understand how these distributions change as a function of the d_{crit} value for the Voronoi technique (and for α with the VWR technique, not shown), six different noise levels for cubic and hexagonal 80 × 80 microstructures were generated and seven different d_{crit} values were performed for each microstructure. Figure 8 shows the evolution of the local PDAS and coordination number distributions as a function of noise level (Figures 8(a) through (f)) and d_{crit} (multiple lines within each subfigure). Each subfigure displays the local PDAS/coordination number statistics in the same manner as that described for the random microstructure (Figure 7). The hypothesis for the following set of cubic microstructures is that as the noise is increased, the standard deviation of the local PDAS/coordination number distributions (i.e., the slope of the distribution functions) increases, but the mean values will tend to reflect that of the base cubic microstructure (i.e., PDAS = 1 and bulk coordination number of 4)—the values of d_{crit} that best capture this might best describe the local statistics.

Several trends are noticeable from the various probability distribution function plots in Figure 8. The first observation is that at low noise levels (e.g., $0.05a_0$) and low d_{crit} values, the PDAS deviates greatly from the standard S-shaped normal distribution curve. This abnormal distribution can be further explained by the local coordination number distribution (right plots, Figure 8). The local coordination number plots in Figure 8 indicate that these conditions cause a significant number of local coordination numbers above 4 to appear (bulk coordination number as high as 6, as noted previously), even though the low noise levels should approach coordination numbers similar to a zero-noise cubic microstructure (i.e., bulk coordination number of 4). Since there is very little noise, these nearest neighbors are likely the diagonal second-nearest neighbors, which have a higher spacing than the four

nearest neighbors in the cubic arrangement; thus, the local PDAS values are heavily influenced by the inclusion of the 5th, 6th, and perhaps higher-numbered neighbors.

A second observation is that the distributions become more similar in shape and symmetric about the mean as the noise is increased, which reflects that the standard deviations of the distributions are similar and the distributions are merely offset by different mean values, which linearly correlate to d_{crit} at higher noise levels. It should be noted that, for every noise level, the higher values of d_{crit} ($= \{0.10, 0.12\}$) tend to approach PDAS = 1—the PDAS of the zero-noise cubic microstructure. The slope of the local PDAS probability distribution is also decreased with higher noise levels for d_{crit} ($= \{0.10, 0.12\}$), i.e., increased noise, increased standard deviation of the local PDAS distribution.

A third observation is that, as the noise level is increased, more local coordination numbers lower than 4 are admitted. This statement is particularly true for higher values of d_{crit}; hence, as d_{crit} is increased, there is a higher probability of admitting local coordination numbers of either 2 or 3. Conversely, as d_{crit} is decreased, there is a higher probability of admitting local coordination numbers of 6 or greater. In terms of the mean behavior, this results in bulk coordination numbers of 4 and 6 for $d_{crit} = 0.12$ and $d_{crit} = 0.00$, respectively. So, for cubic microstructures with varying degrees of noise, d_{crit} values of 0.10 or 0.12 yields local PDAS and coordination numbers that are consistent with the zero-noise cubic microstructure, while displaying an increase in the standard deviation of the distribution with increasing noise, as would be expected.

2. Voronoi technique with hexagonal microstructures

The same sort of probability distribution plots are shown for hexagonal microstructures in Figure 9. Again, the hypothesis is that as the noise within the microstructure is increased, the PDAS should still trend towards 1 and the local coordination number should be approximately 6, but the standard deviation of the distribution will increase. There are a few interesting observations that contrast those with the cubic microstructures.

First, in the case of low values of d_{crit}, there is not the same abnormal behavior at low noise levels as with the
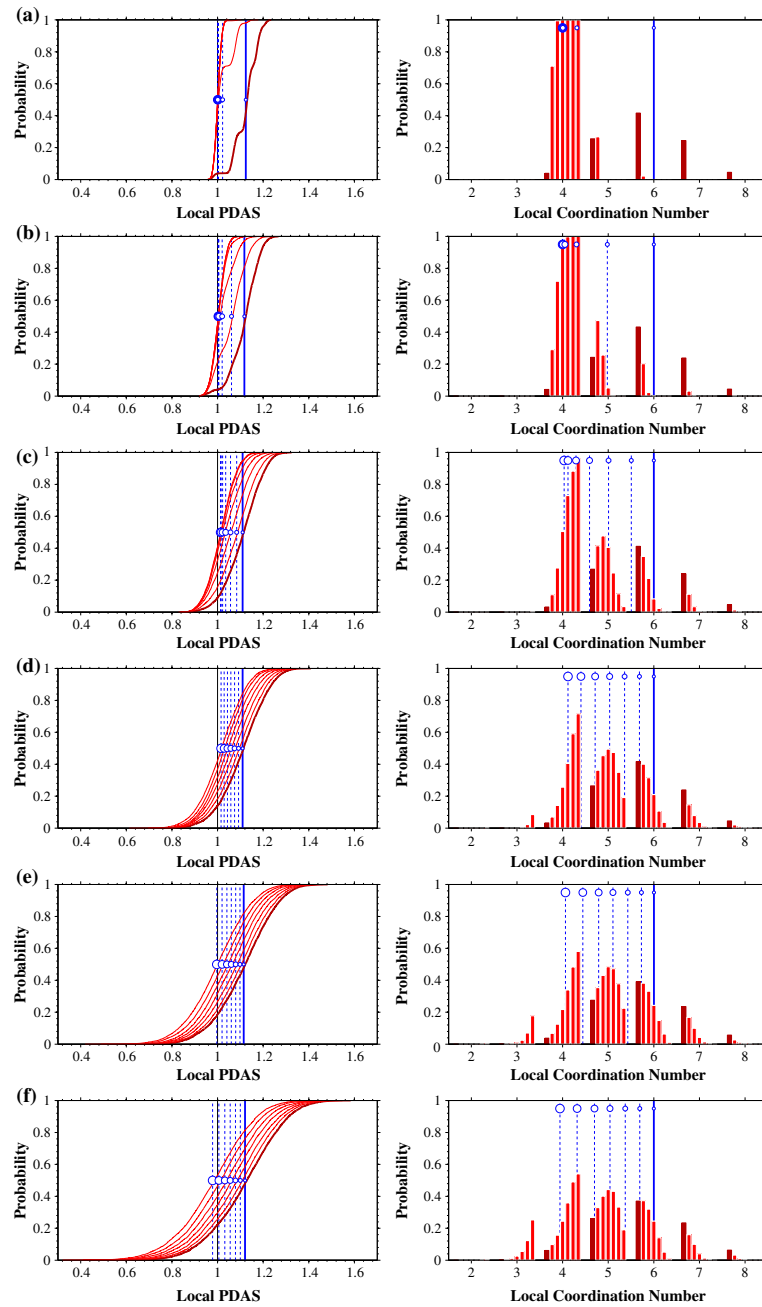
Fig. 8—Cumulative probability plot of the local PDAS (left plot) and coordination number (right plot) distribution as a function of the parameter d_{crit} for the Voronoi method for cubic microstructures (80 × 80) with different noise levels: (*a*) $0.05a_0$, (*b*) $0.10a_0$, (*c*) $0.20a_0$, (*d*) $0.30a_0$, (*e*) $0.40a_0$, and (*f*) $0.50a_0$. The red (dotted blue) line represents the local PDAS/coordination number distribution (bulk PDAS/coordination number) for d_{crit} values of 0.00 (right, thick line) to 0.12 (left) in increments of 0.02.

METALLURGICAL AND MATERIALS TRANSACTIONS A
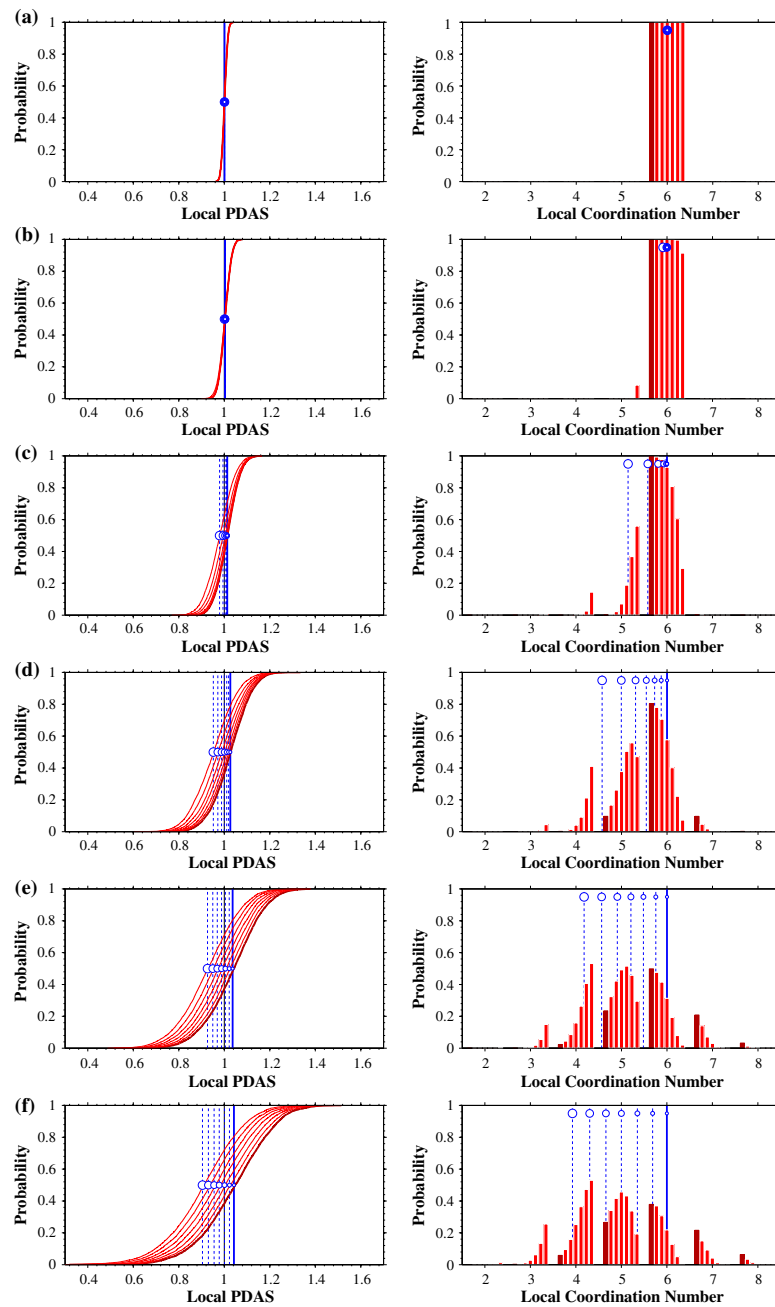
VOLUME 46A, OCTOBER 2015—4621

48

Fig. 9—Cumulative probability plot of the local PDAS (left plot) and coordination number (right plot) distribution as a function of the parameter d_{crit} for the Voronoi method for hexagonal microstructures (80 × 80) with different noise levels: (*a*) 0.05a_0, (*b*) 0.10a_0, (*c*) 0.20a_0, (*d*) 0.30a_0, (*e*) 0.40a_0, and (*f*) 0.50a_0. The red (dotted blue) line represents the local PDAS/coordination number distribution (bulk PDAS/coordination number) for d_{crit} values of 0.00 (right, thick line) to 0.12 (left) in increments of 0.02.

cubic microstructures. This is perhaps an expected result, because the six nearest neighbors effectively shield the second-nearest neighbors, which enabled the abnormal behavior in the distributions for the cubic microstructures. For the same small noise levels with the hexagonal microstructures, there is also very little difference between the local PDAS or the local coordination number distributions compared to that observed within the cubic microstructures.

Second, as the noise in increased within the hexagonal microstructure, the spread of the bulk PDAS and bulk coordination numbers increased. However, in contrast to the cubic microstructures, the bulk PDAS values drop below PDAS = 1 and a lower value of $d_{crit} = 0.04$ or $d_{crit} = 0.06$ is actually closer to the ideal-hexagonal-microstructure PDAS value.

Third, the tendency is for lower coordination numbers to be calculated with increasing noise in the microstructure and with increasing d_{crit} values. For the highest noise level explored herein, the extreme bulk coordination numbers are 4 and 6 for $d_{crit} = 0.12$ and $d_{crit} = 0.00$, respectively. Interestingly, these bulk coordination numbers are nearly identical to those of the cubic microstructures with the highest noise level—so there may be a convergence in the behavior of the Voronoi technique with respect to the higher noise levels of the microstructure. For smaller noise levels in the cubic and hexagonal microstructures, d_{crit} values between 0.04 and 0.12 give reasonable behavior in comparison to the known values from a zero-noise microstructure.

3. Voronoi Warnken–Reed technique

The same analysis was also conducted to examine the variability due to the noise level and the parameter α within the VWR technique. The subsequent plots are attached in Appendix. What is immediately apparent is that a large fraction of points have a calculated coordination number of 3 using this technique, irrespective of noise level and even α value. Recall that this is an initial parameter that is set within the VWR method, whereby the three nearest neighbors were initially selected to calculate the standard deviation and then this value is used with α to decide on the next-closest neighbor—an initial value of 2 is too few for a standard deviation calculation and a value of 4 eliminates the possibility of local coordination numbers with values less than 4. Moreover, the bulk coordination number never exceeds a value of 4.5, even with $\alpha = 2.0$, for hexagonal structures (even at low noise levels). This finding indicates that this distance-based technique is certainly underestimating the coordination number in hexagonal microstructures, i.e., compare Figure A2 in Appendix with Figure 9 to compare techniques for the exact same microstructure. In a distance-based technique such as this, the addition of these nearest neighbors always increases the local PDAS. Hence, the larger α is for the VWR, the more skewed the local PDAS distribution is towards higher local PDAS values.

D. Local Correlation for Different Parameters

The subsequent datasets can also be analyzed to examine the correlation between local PDAS and local coordination numbers. This sort of analysis can help answer the question "is there a high degree of correlation between the local PDAS values for different technique parameter values?" Another valid question is that of "is there a high degree of correlation between the local PDAS values and the local coordination numbers for different technique parameter values?" Both of the aforementioned questions are subsequently addressed in the next two subsubsections.

1. Local PDAS correlation

Figure 10 shows a few examples of correlations between the local PDAS values for two different methods—(a) Voronoi method and (b) VWR method—using two different parameter values (d_{crit} of $\{0.00, 0.12\}$ and α of $\{1.0, 2.0\}$, respectively). These scatter plots combine all of the various 80 × 80 cubic and hexagonal microstructures explored in Section III–C. The scatter plots were incrementally plotted such that the largest noise level was plotted, then the second largest, etc. In this manner, the lower-noise data points are plotted over higher-noise data points, but overall this plot identifies the degree of randomness or bias between the two parameters chosen for the same technique. Note that each data point represents the technique being applied to the same point with the same local environment.

There are some similarities and differences for the correlation plots in Figure 10. Since the colors in these plots indicate the different noise levels, it is observed that the larger noise levels result in a larger spread of the PDAS values, as would be expected from the previous analyses conducted herein. In both cases, though, there is not a linear correlation between the two different parameter levels, i.e., knowing the local PDAS at one point for a given parameter level is insufficient information to predict the local PDAS at that same point with a different parameter level for the same technique.

Some of the differences are as follows. First, notice that the Voronoi technique in Figure 10(a) has some values that lie above the 45 deg line. This indicates that in some cases, the Voronoi technique with a higher d_{crit} will, in fact, exclude some closer local PDAS values, which causes the local PDAS value to increase with increasing d_{crit}. However, this situation is not a common occurrence, as can be observed from the majority of points that lie below this line. This behavior contrasts the VWR technique in Figure 10, which has all local PDAS values either on the 45 deg line or above it. Of course, this is as expected since the VWR is a distance-based technique, so an increased α results in either the same number of nearest neighbors (and local PDAS) or a higher number of neighbors (with a larger local PDAS). Second, at low noises (blue and light blue data points), the Voronoi method starts to deviate from the expected linear correlation between the two d_{crit} values. This behavior is caused by $d_{crit} = 0.0$ counting nearest neighbors that have moved further away, thus biasing
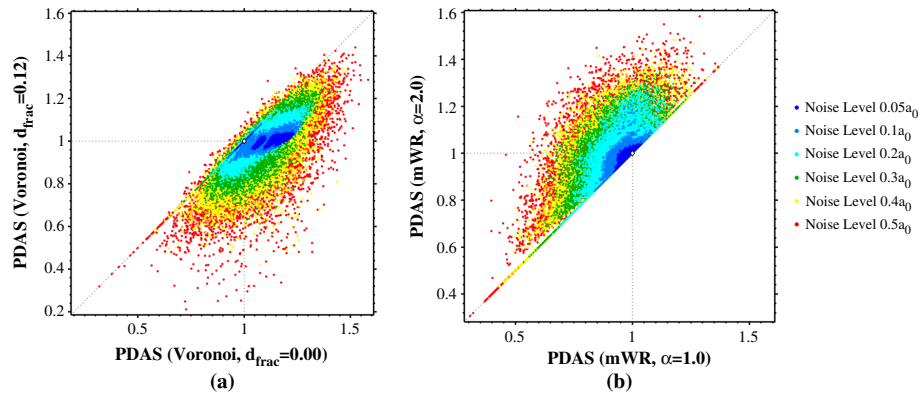
Fig. 10—Scatter plot of the correlation between the local PDAS for two different methods—(*a*) Voronoi method and (*b*) Voronoi Warnken–Reed method—using two different parameter values (d_{crit} of $\{0.00, 0.12\}$ and α of $\{1.0, 2.0\}$, respectively). These scatter plots combine all of the various 80×80 cubic and hexagonal microstructures explored in Section III–C and the colors correspond to the different microstructure noise levels (see legend on right).
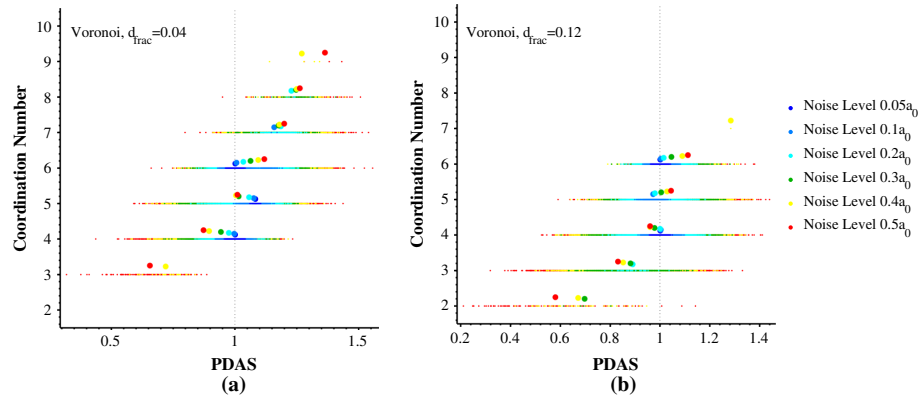

Fig. 11—Scatter plot of the correlation between the local PDAS values and the local coordination numbers for Voronoi method with two different parameter values: d_{crit} of (*a*) 0.04 and (*b*) 0.12. These scatter plots combine all of the various 80×80 cubic and hexagonal microstructures explored in Section III–C and the colors correspond to the different microstructure noise levels (see legend on right). The larger offset dots indicate the bulk PDAS values as a function of noise level and the (nearest) coordination number.

the local PDAS by including these points—this is especially evident for the case of cubic microstructures where second-nearest neighbors are counted for $d_{crit} = 0.0$. On the other hand, the higher d_{crit} value instead excludes these further points and maintains a local PDAS of 1.0, in agreement with the zero-noise microstructure.

2. *Local PDAS and local coordination number correlation*

Figure 11 shows a few examples of correlations between the local PDAS values and the local coordination numbers for Voronoi method with two different parameter values (d_{crit} of $\{0.04, 0.12\}$). These scatter plots are similar to Figure 10 in that they combine all of the various 80×80 cubic and hexagonal microstruc-

tures explored in Section III–C. The scatter plots were incrementally plotted form the largest noise level to the smallest in a similar manner. However, the coordination numbers are discrete values, so the scatter plot takes on a different form. In order to understand how the bulk PDAS is also evolving within each coordination number, a larger circle marker symbol is included above each discrete coordination number to indicate this trend.

There are some trends that emerge from the correlation plots in Figure 11. In general, increasing local coordination number results in higher local and bulk PDAS values. Local coordination numbers of 4, 5, and 6 are common over all noise levels and both d_{crit} values, with some lower and higher local coordination numbers occurring with an increase in the noise of the mi-

crostructure. In general, the higher d_{crit} values results in lower local coordination numbers and, consequently, lower PDAS values. In terms of the bulk PDAS behavior with respect to the individual coordination numbers, two coordination number regimes are observed: (1) For coordination numbers less than 5, the bulk PDAS decreases with increasing noise level, and (2) for coordination numbers greater than 5, the bulk PDAS increases with increasing noise level. In both cases, the general trend is that the bulk PDAS for each coordination number will move further away from PDAS = 1.0 with increasing noise in the microstructure. The only exception is for the coordination number of 5, which is a function of the competing influences from the cubic (coordination number of 4) and hexagonal (coordination number of 6) microstructures.

IV. CONCLUSIONS

In this work, four series of simulations using cubic and hexagonal synthetic microstructures with varying degrees of noise were utilized to study the effects of length scale, base microstructure, microstructure variability, and technique parameters on the local PDAS distribution, local coordination number distribution, bulk PDAS, and bulk coordination number (calculated as the mean of the local statistics). The length scale study used 20 instantiations to identify a size of our synthetic microstructure whereby the variability in the mean statistics starts to converge—an 80×80 microstructure (*i.e.*, 6400 dendrites) was chosen herein. While a number of the quantitative findings are detailed herein, a few important findings help to evaluate the relative capability of these approaches to quantify theses local statistics.

1. For the Voronoi tesselation technique, utilizing the d_{crit} (polygon-side-length) criterion ($d_{crit} \geq 0.04$) was necessary to correctly capture bulk coordination numbers for cubic and hexagonal microstructures with small amounts of disorder (noise).
2. For the VWR method, the α parameter in the range examined herein is not able to capture the bulk coordination numbers for hexagonal microstructures with small amounts of noise, signifying that it may significantly under-predict coordination numbers for hexagonal dendritic configurations (which results in under-predicting the PDAS statistics as well).
3. The subsequent analysis of the local coordination numbers and local PDAS distributions identifies a number of trends in the local distributions that help explain the behavior of these techniques and their bulk-calculated statistics. In general, the right

trends are observed—with increasing noise in the microstructures, the Voronoi technique correctly captures the increasing standard deviation of the local PDAS distribution.
4. In terms of the correlation study, there is not a clear linear correlation between different d_{crit} values for the local statistics; this may be partly associated with the general (weak, but clearly evident) trend that an increase in the local coordination number tends to increase the local PDAS value.

Overall, the Voronoi tesselation technique with the d_{crit} (polygon-side-length) criterion best captures the wide range of directionally solidified dendritic microstructures. This systematic study of the different techniques for quantifying local primary dendrite arm spacings evaluates their capability to capture this important microstructure feature in different synthetically derived dendritic microstructures, which can be an important step for correlating with both processing and properties in directionally solidified microstructures, such as in single crystal nickel-based superalloys.

APPENDIX

Figures A1 and A2 present data pertaining to how the local PDAS and coordination number distributions change as a function of the α value for the VWR technique. Six different noise levels for cubic and hexagonal 80×80 microstructures were generated (Figures A1 and A2, respectively) and 11 different α values were performed for each microstructure. The α values were incremented from 1.0 to 2.0 in increments of 0.1 for the subsequent analysis. All other aspects are similar in nature to Figures 7, 8, and 9, which show the evolution of these local distributions with d_{crit} for the Voronoi technique. Further discussion of these plots and their results is in Section III–C–3.

Fig. A1—Cumulative probability plot of the local PDAS (left plot) and coordination number (right plot) distribution as a function of the parameter α for the Voronoi Warnken–Reed method for cubic microstructures (80 × 80) with different noise levels: (a) $0.05a_0$, (b) $0.10a_0$, (c) $0.20a_0$, (d) $0.30a_0$, (e) $0.40a_0$, and (f) $0.50a_0$. The red (dotted blue) line represents the local PDAS/coordination number distribution (bulk PDAS/coordination number) for α values of 0.00 (right, thick line) to 0.12 (left) in increments of 0.02.
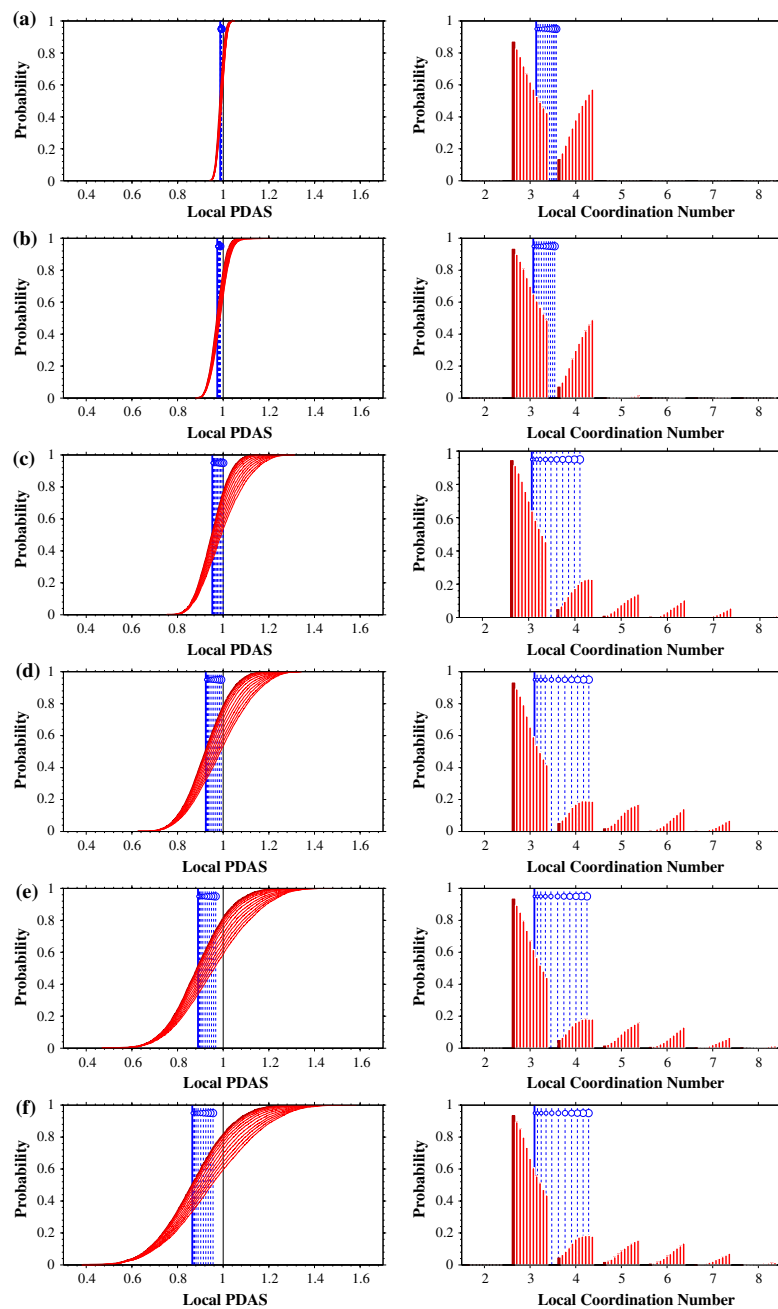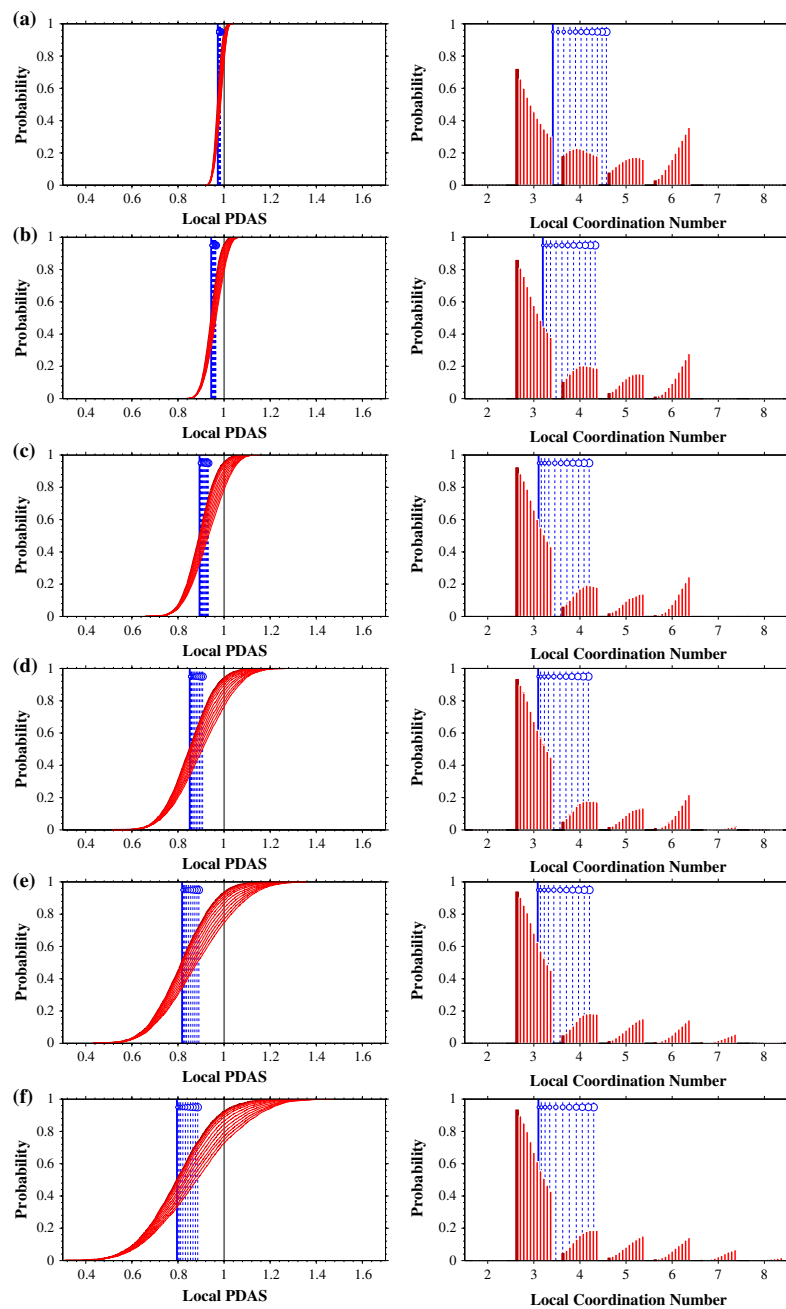
Fig. A2—Cumulative probability plot of the local PDAS (left plot) and coordination number (right plot) distribution as a function of the parameter α for the Voronoi Warnken–Reed method for hexagonal microstructures (80 × 80) with different noise levels: (a) $0.05a_0$, (b) $0.10a_0$, (c) $0.20a_0$, (d) $0.30a_0$, (e) $0.40a_0$, and (f) $0.50a_0$. The red (dotted blue) line represents the local PDAS/coordination number distribution (bulk PDAS/coordination number) for α values of 0.00 (right, thick line) to 0.12 (left) in increments of 0.02.

REFERENCES

1. R.C. Reed: *The Superalloys: Fundamentals and Applications*, Cambridge University Press, 2006.
2. T.M. Pollock and S. Tin: *J. Propul. Power*, 2006, vol. 22, pp. 361–74.
3. H.S. Whitesell and R.A. Overfelt: *Mater. Sci. Eng. A*, 2001, vol. 318, pp. 264–76.
4. A.J. Elliott, S. Tin, W.T. King, S.C. Huang, M.F.X. Gigliotti, and T.M. Pollock: *Metall. Mater. Trans. A*, 2004, vol. 35A, pp. 3221–31.
5. M.L.N.M. Melo, E.M.S. Rizzo, and R.G. Santos: *J. Mater. Sci.*, 2005, vol. 40, pp. 1599–1609.
6. M. Lamm and R.F. Singer: *Metall. Mater. Trans. A*, 2007, vol. 38A, pp. 1177–83.
7. C.L. Brundidge, D. Vandrasek, B. Wang, and T.M. Pollock: *Metall. Mater. Trans. A*, 2012, vol. 43A, pp. 965–76.
8. P.N. Quested and M. McLean: *Mater. Sci. Eng.*, 1984, vol. 65, pp. 171–80.
9. V.A. Wills and D.G. McCartney: *Mater. Sci. Eng. A*, 1991, vol. 145, pp. 223–32.
10. D.G. McCartney and J.D. Hunt: *Acta Metall.*, 1981, vol. 29, pp. 1851–63.
11. L. Li and R.A. Overfelt: *J. Mater. Sci.*, 2002, vol. 37, pp. 3521–32.
12. J. Hui, R. Tiwari, X. Wu, S.N. Tewari, and R. Trivedi: *Metall. Mater. Trans. A*, 2002, vol. 33A, pp. 3499–10.
13. W. Wang, P.D. Lee, and M. McLean: *Acta Mater.*, 2003, vol. 51, pp. 2971–87.
14. J.D. Miller and T.M. Pollock: *Development and Application of an Optimization Protocol for Directional Solidification: Integrating Fundamental Theory, Experimentation and Modeling Tools*, Wiley, pp. 653–62, Superalloys 2012.
15. C.L Brundidge, J.D. Miller, and T.M. Pollock: *Metall. Mater. Trans. A*, 2011, vol. 42A, pp. 2723–32.
16. L. Liu, T.W. Huang, J. Zhang, and H.Z. Fu: *Mater. Lett.*, 2007, vol. 61, pp. 227–30.
17. F. Wang, D.X. Ma, J. Zhang, S. Bogner, and A. Buhrig-Polaczek: *J. Mater. Process. Technol.*, 2014, vol. 214, pp. 3112–21.
18. B.C. Wilson, E.R. Cutler, and G.E. Fuchs: *Mater. Sci. Eng. A*, 2008, vol. 479, pp. 356–64.
19. A.F. Giamei and J.G. Tschinkel: *Metall. Trans. A*, 1976, vol. 7, pp. 1427–34.
20. A. Lohmüller, W. Eßer, J. Großmann, M. Hördler, J. Preuhs, and R.F. Singer: in *Superalloys 2000*, T.M. Pollock, R.D. Kissinger, R.R. Bowman, K.A. Green, M. McClean, S. Olson, and J.J. Schirra, eds., The Minerals, Metals & Materials Society (TMS), 2000 pp. 181–88.
21. M.M. Franke, R.M. Hilbinger, A. Lohmüller, and R.F. Singer: *J. Mater. Process. Technol.*, 2013, vol. 213, pp. 2081–88.
22. T. Zhang, W.L. Ren, J.W. Dong, X. Li, Z.M. Ren, G.H. Cao, Y.B. Zhong, K. Deng, Z.S. Lei, and J.T. Guo: *J. Alloys Compd.*, 2009, vol. 487, pp. 612–17.
23. X. Li, Z.M. Ren, J. Wang, Y.F. Han, and B.D. Sun: *Mater. Lett.*, 2012, vol. 67, pp. 205–209.
24. W.D. Xuan, Z.M. Ren, and C.J. Li: *J. Alloys Compd.*, 2015, vol. 620, pp. 10–17.
25. M.A. Tschopp, M.A. Groeber, R. Fahringer, J.P. Simmons, A.H. Rosenberger, and C. Woodward: *Scripta Mater.*, 2010, vol. 62, pp. 357–60.
26. S.N. Tewari, R.N. Grugel, and D.R. Poirier: *Metall. Mater. Trans. A*, 2014, vol. 45A, pp. 4758–61.
27. S. Tewari, R. Grugel, and D. Poirier: *Metall. Mater. Trans. A*, 2014, vol. 45A, pp. 4758–61.
28. M.C. Flemings: *Metall. Trans.*, 1974, vol. 5, pp. 2121–34.
29. H. Jacobi and K. Schwerdtfeger: *Metall. Trans. A*, 1976, vol. 7A, pp. 811–20.
30. X.B. Zhao, L. Liu, W.G. Zhang, Z.H. Yu, and H.Z. Fu: *Mater. Chem. Phys.*, 2011, vol. 125, pp. 55–58.
31. S.N. Tewari, Y.H.S. Weng, G.L. Ding, and R. Trivedi: *Metall. Mater. Trans. A*, 2002, vol. 33A, pp. 1229–43.
32. U. Paul, P.R. Sahm, and D. Goldschmidt: *Mater. Sci. Eng. A*, 1993, vol. 173, pp. 49–54.
33. M.A. Tschopp, J.D. Miller, A.L. Oppedal, and K.N. Solanki: *Metall. Mater. Trans. A*, 2014, vol. 45A, pp. 426–37.
34. J.D. Miller: Ph.D. Thesis, University of Michigan, 2011.
35. M.A. Tschopp, G.B. Wilks, and J.E. Spowart: *Modell. Simul. Mater. Sci. Eng.*, 2008, vol. 16, p. 065009.
36. N. Warnken and R.C. Reed: *Metall. Mater. Trans. A*, 2011, vol. 42A, pp. 1675–83.
37. N. Warnken and R.C. Reed: *IOP Conference Series: Materials Science and Engineering*, 2011, vol. 27 pp. 1–5.

1.

1. Report Type

Final Report

Primary Contact E-mail
Contact email if there is a problem with the report.

aoppedal@cavs.msstate.edu

Primary Contact Phone Number
Contact phone number if there is a problem with the report

662.325.8502

Organization / Institution name

Mississippi State University

Grant/Contract Title
The full title of the funded effort.

Hierarchically-driven approach for quantifying uncertainty in creep deformation and failure of aerospace materials

Grant/Contract Number
AFOSR assigned control number. It must begin with "FA9550" or "F49620" or "FA2386".

FA9550-12-1-0135

Principal Investigator Name
The full name of the principal investigator on the grant or contract.

Andrew L. Oppedal

Program Manager
The AFOSR Program Manager currently assigned to the award

James M. Fillerup

Reporting Period Start Date

04/01/2012

Reporting Period End Date

03/31/2016

Abstract

In collaboration with AFRL colleagues we have developed a methodology for measuring localized microstructure metrics in dendritic microstructures such as single crystal nickel-based superalloys, with potential application to a wide range of material systems. The primary dendrite arm spacing is correlated to processing (solidification rate), the microstructure of the material (interdentritic eutectic particles and voids), and properties (fatigue behavior and creep strength). In this project a Voronoi-based approach for spatial point pattern analysis has been applied to experimental and synthetic dendritic microstructures. This technique was used to quantify the distribution of local primary dendrite arm spacings, their spatial distribution, and their correlation with interdentritic eutectic particles. Several peer-reviewed journal articles, including an Editor's Choice article published in Metallurgical and Materials Transactions, and conference presentations describe this in more detail. Furthermore, to transfer this technology, a GUI based computational too has been developed to facilitate the use of these metrics in synthetic and experimental microstructures, with eventual application to link processing with structural properties based on the complex turbine blade microstructure.

Distribution Statement
This is block 12 on the SF298 form.

DISTRIBUTION A: Distribution approved for public release.

Distribution A - Approved for Public Release

Explanation for Distribution Statement

If this is not approved for public release, please provide a short explanation. E.g., contains proprietary information.

SF298 Form

Please attach your SF298 form. A blank SF298 can be found here. Please do not password protect or secure the PDF The maximum file size for an SF298 is 50MB.

sf298_FA9550-12-1-0135.pdf

Upload the Report Document. File must be a PDF. Please do not password protect or secure the PDF . The maximum file size for the Report Document is 50MB.

FA9550-12-1-0135_AFOSR_Final_Report.pdf

Upload a Report Document, if any. The maximum file size for the Report Document is 50MB.

Archival Publications (published) during reporting period:

M.A. Tschopp, A.L. Oppedal, J.D. Miller, M.A. Groeber, A.H. Rosenberger, K.N. Solanki, Characterizing primary dendritic microstructures to quantify the processing-structure-property relationship in single crystal nickel-based superalloys, in: TMS Annual Meeting, 2013: pp. 301–310.

M.A. Tschopp, J.D. Miller, A.L. Oppedal, K.N. Solanki, Characterizing the Local Primary Dendrite Arm Spacing in Directionally Solidified Dendritic Microstructures, Metall and Mat Trans A. 45 (2014) 426–437.

M.A. Tschopp, J.D. Miller, A.L. Oppedal, K.N. Solanki, Evaluating Local Primary Dendrite Arm Spacing Characterization Techniques Using Synthetic Directionally Solidified Dendritic Microstructures, Metallurgical and Materials Transactions A. 46 (2015) 4610–4628.

2. New discoveries, inventions, or patent disclosures:

Do you have any discoveries, inventions, or patent disclosures to report for this period?

No

Please describe and include any notable dates

Do you plan to pursue a claim for personal or organizational intellectual property?

Changes in research objectives (if any):

Change in AFOSR Program Manager, if any:

PM April 2012 through October 2015: David S. Stargel, AFOSR
PM November 2015 through March 2016: James M. Fillerup, AFOSR

Extensions granted or milestones slipped, if any:

A 12 month No Cost Extension was approved by AFOSR on 30 March 2015

AFOSR LRIR Number

LRIR Title

Reporting Period

Laboratory Task Manager

Program Officer

Research Objectives

Technical Summary

Funding Summary by Cost Category (by FY, $K)

	Starting FY	FY+1	FY+2
Salary			
Equipment/Facilities			
Supplies			
Total			

Report Document

Report Document - Text Analysis

Report Document - Text Analysis

Appendix Documents

2. Thank You

E-mail user

Jun 30, 2016 16:34:49 Success: Email Sent to: aoppedal@cavs.msstate.edu